MODELING AND OPTIMIZATION OF POLYMER COMPOSITE-STEEL CONSTRUCTION MATS AND THEIR POTENTIAL APPLICATION TO OCEAN ENGINEERING STRUCTURES

A Thesis

by

PARKER TRAVIS RODRIGUES

Submitted to the Office of Graduate and Professional Studies of
Texas A&M University
in partial fulfillment of the requirements for the degree of

MASTER OF SCIENCE

Chair of Committee,	David H. Allen
Committee Members,	HeonYong Kang
	Ray W. James
Head of Department,	Sharath Girimaji

May 2020

Major Subject: Ocean Engineering

ABSTRACT

Construction mat design is currently experiencing an update to modern polymer composite materials. The new designs lack optimization, sacrificing structural integrity for cost of production or vice versa. This thesis focuses on the optimization of polymer composite-steel construction mats via a multicomponent model. Model components include an analytical model, formulated via Euler-Bernoulli beam theory, and a series of both 3-D and 2-D finite element models to approximate local and global structural abilities. Modeling validation stemmed from available experimental data. Optimization is achieved by comparing structural design against material costs. Additionally, potential application of resulting design to ocean engineering structures, namely coastal infrastructure, is explored.

CONTRIBUTORS AND FUNDING SOURCES

Contributors

This work was supervised by a thesis committee consisting of Professors David. H. Allen [advisor] and HeonYong Kang of the Department of Ocean Engineering and Professor Ray W. James of the Department of Civil Engineering.

The data analyzed for Chapter 1 was provided by Professor David H. Allen. All other work conducted for the thesis was completed by the student independently.

Funding Sources

There are no outside funding contributions to acknowledge related to the research and compilation of this document.

TABLE OF CONTENTS

PAGE

LIST OF FIGURES

PAGE

LIST OF TABLES

INTRODUCTION

Construction mat design has recently undergone an update to modern, engineered materials. These new-to-market construction mats, still in product-infancy in comparison to traditional designs, are in need of further optimization to make them a superior alternative amongst their market competitors.

Construction mats, whether modern or traditional, are comprised of beam components fastened together to form a working platform. These mats are also commonly referred to as crane mats, access mats, timber mats, digging mats, or bridge mats. Reusable and relocatable, construction mats are purpose-built as work platforms for equipment such as cranes and large stationary pumps, or implemented as general temporary infrastructure e.g. an access road for excavation and earth-moving. These mats must be able to adapt and operate in all environments, with both ideal and nonideal working conditions. Overall, these mats aid in the efficient and safe completion of construction projects, while leaving minimal impact on the worksite and surrounding environment. Figure 1 below depicts typical construction mat usage.

Figure 1 Example operation of construction mat

In traditional construction mats, the primary beam components consist of milled hardwoods. Depending on specific application, secondary reinforcing beam components may also be incorporated into the mat in the form of steel interleaves, also known as flitch plates. Fastening of the beam elements is accomplished mechanically (nut and bolt), chemically (laminated), or both. A cross-section view of a typical traditional construction mat design is presented below in Figure 2.

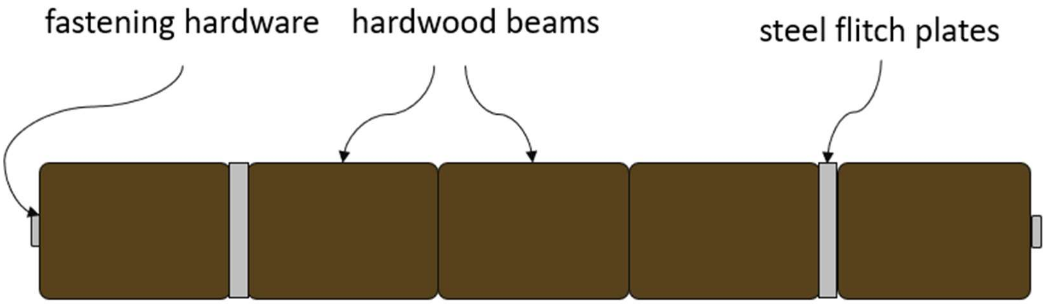

Figure 2 Cross-section view of traditional construction mat design

Modern construction mats are seeing an update in material choice of the primary beam components. Readily available polymer composites offer a vastly superior primary beam component alternative compared to current hardwoods. Hardwoods yield and or fail under lower magnitude loads relative to available polymer composites, and fatigue faster under cyclical loading (*Wood handbook: wood as an engineering material,* 2011*)*. Additionally, they degrade at substantially higher rates in working environments, especially with common saturated conditions, creating little to no ability for reuse across multiple projects. On the other hand, polymer composites are comparable in raw materials and manufacturing costs, but retain more value in the long-term with the superior operational ability and durability described above. Moreover, ease of manufacture of the polymer composites allows for not only standard modular configurations similar to traditional hardwood mats, but also purpose-designed configurations for specific project needs. From an environmental standpoint, chemically stable and inert polymer composites, many containing at least some partially recycled constituents, provide a much more sustainable alternative to hardwoods. With all of the above benefits of new polymer composite materials in construction mats, design life for the structures has been extended. No longer a structure to be used, abused, and thrown away on a per project basis, it is now viable and necessary to maximize the structural integrity of the modern construction mat.

To accomplish the above task, an optimization was carried out on a typical mat structure, parameterizing structural integrity against materials costs. Optimization efforts were accomplished via the formulation of a multicomponent model. The components of this model included: experimental testing and resulting data, an analytical model, and various numerical, finite element models. Modeling and optimizations were tailored to the available experimental data for purposes of this thesis. However, it should be noted that the overall modeling and optimization procedure established here is more widely applicable to elastic behavior of any general construction mat design that utilizes discreet homogeneous components.

POTENTIAL APPLICATION TO OCEAN ENGINEERING STRUCTURES

Given the superior material and structural properties polymer composite-steel construction mats provide, and the simple yet robust modular design they possess, an easy translation can be made to Ocean Engineering structures. Specifically, the respective structure could be a cost-effective alternative to many coastal infrastructure applications. These applications include seawalls and port/harbor installations. An example of a contemporary seawall structure and port/harbor installation are pictured below in Figures 3 and 4.

Figure 3 Contemporary seawall

Figure 4 Contemporary port/harbor installation, quay wall

Coastal regions are highly morphological in nature making implementation of any infrastructure very site-specific. Additionally, the environment presents taxing loading situations, with constant random waves, frequent storm events, and highly corrosive saltwater. The implementation of the structure contained in this thesis would present several advantages for the above coastal infrastructure application. First, adaption of the structure to fit most site-specific needs would be easy and cost effective. An example of this would be a variable minimum depth needed for a seawall installation to fit local soil conditions and accompanying moisture diffusion conditions. Current use of reinforced concrete walls, pictured in Figure 3 above, present significantly large installation costs in comparison to the easy manufacture of unit mat segments with different required lengths. Another example of this, related to Figure 4 above, would be the use of the mat structure as a quay wall, where high frequency of docking ships presents the need for a modular, cheap, easily replaced/installed structure, which the mat would readily provide. Lastly, with regards to any possible coastal infrastructure application, the inert, stable, and partially recycled materials the mat is comprised of, would provide not only a long-lasting salt-water resilient structure, but also an environmentally friendly solution. Overall, the mat structure detailed in this thesis could provide a unique and superior infrastructure alternative for coastal environments.

MODELING METHODOLOGY

Optimization efforts of the construction mat design were centered around development, validation and employment of a multicomponent model. The components of the model included: experimental testing and resulting data, an analytical model formed via Euler-Bernoulli beam theory and validated against the experimental data, and various numerical finite element models, also validated against the experimental data. Altogether, the components of the model formed the predictive tools that were later used in optimization efforts.

EXPERIMENTAL TESTING

Experimental data was needed to serve as a foundation for modeling efforts and later, validation purposes. Experimental data was sourced and utilized from full-scale four-point bend tests completed on several configurations of a commercially available modern construction mat. Testing was completed at Texas A&M University's High-Bay Lab, under the purview of the Center for Railway Research. Figure 5 below shows photographic documentation of one of the tests, post-failure.

Figure 5 Photographic documentation of experimental four-point bend test, post-failure

Testing included six different mat configurations; all utilized primary beam components made of a glass fiber-high density polyethylene (HDPE) polymer composite, and secondary beam components made of A36 structural steel. Beam components in all six configurations were mechanically fastened with specialized nut and bolt hardware. Two of the configurations tested were composed solely of polymer composite primary beam components. The other four configurations tested included both polymer composite primary beam components, and steel interleaves. Table 1 below lists the six different configurations of mats, along with key geometric attributes of each.

Mat Desig.	**Beam Height [in.]**	**Beam Width [in.]**	**Steel Plate no./Thick. [in.]**	**Number of Beams**	**Approx. Mat Width [in.]**	**Mat Length [ft]**	**# tests**
(7x9) x 5 x (NS)	**7 1/16**	**8 15/16**	**None**	**5**	**45**	**18**	**2**
(9x7) x 7 x (NS)	**8 15/16**	**7 1/16**	**None**	**7**	**49**	**18**	**2**
(7x9) x 5 x (4x¼)	**7 1/16**	**8 15/16**	**4x1/4**	**5**	**46**	**20**	**3**
(7x9) x 5 x (4x½)	**7 1/16**	**8 15/16**	**4x1/2**	**5**	**47**	**20**	**3**
(9x7) x 7 x (6x¼)	**8 15/16**	**7 1/16**	**6x1/4**	**7**	**50.5**	**20**	**3**
(9x7) x 7 x (4x½)	**8 15/16**	**7 1/16**	**4x1/2**	**7**	**51**	**24**	**4**

Table 1 Configurations and essential geometric properties of experimentally tested construction mats

It should be noted that all glass fiber-HDPE beams used in all configurations were manufactured with a seven and 1/16 inch by eight and 15/16 inch (7.0625”x8.9375”) cross-sectional area, with a one-inch radius on all corners. The primary beam components have a uniform cross section. The *7* or *9* listed at the beginning of each mat designation refers to the vertical orientation of the glass fiber-HDPE beam in the respective configuration. An example cross-sectional depiction of the primary beam components in all configurations, with a *9* orientation is shown below in Figure 6, to aid reader interpretation.

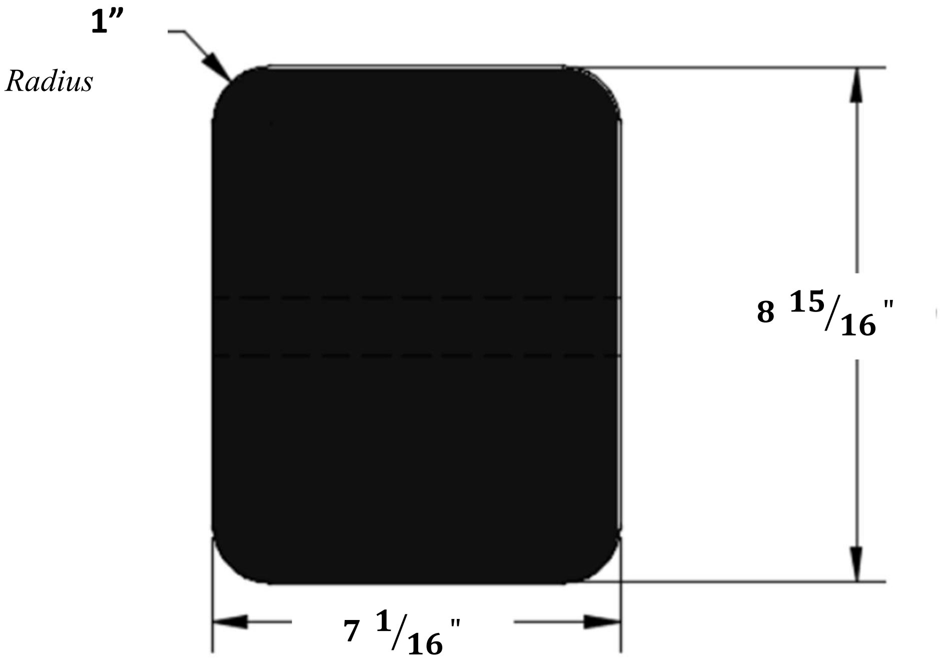

Figure 6 Cross section of primary beam component with *9* orientation

The full mat designation for each configuration is as follows:

(Cross Section Dimensions of Primary Beam, vertical orientation first) x Total # of primary beam comps. x (Number of steel flitch plates x Thickness of steel flitch plate, or NS for no steel)

Each configuration was comprised of different orientations and numbers of polymer composite beams, along with four of the six configurations using either ½” or ¼” steel flitch plates interlaid between the glass fiber-HDPE beams. Note that not all configurations contained consistent alternation of polymer composite beams to steel flitch plates. Steel flitch plates were also one inch shorter in height than the adjacent polymer composite beam components. For example, isometric and cross-sectional depictions of mat configurations *(7x9) x 5 x (4x½)* and *(9x7) x 7 x (4x½)* are presented in Figures 7-10.

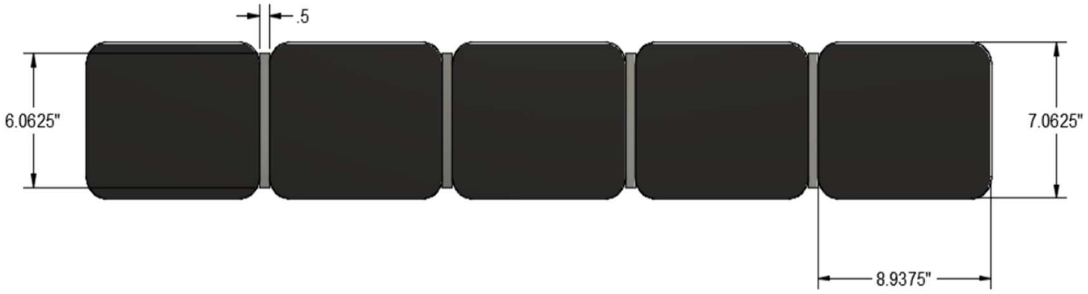

Figure 7 Cross section, (7x9) x 5 x (4x½) experimental mat configuration

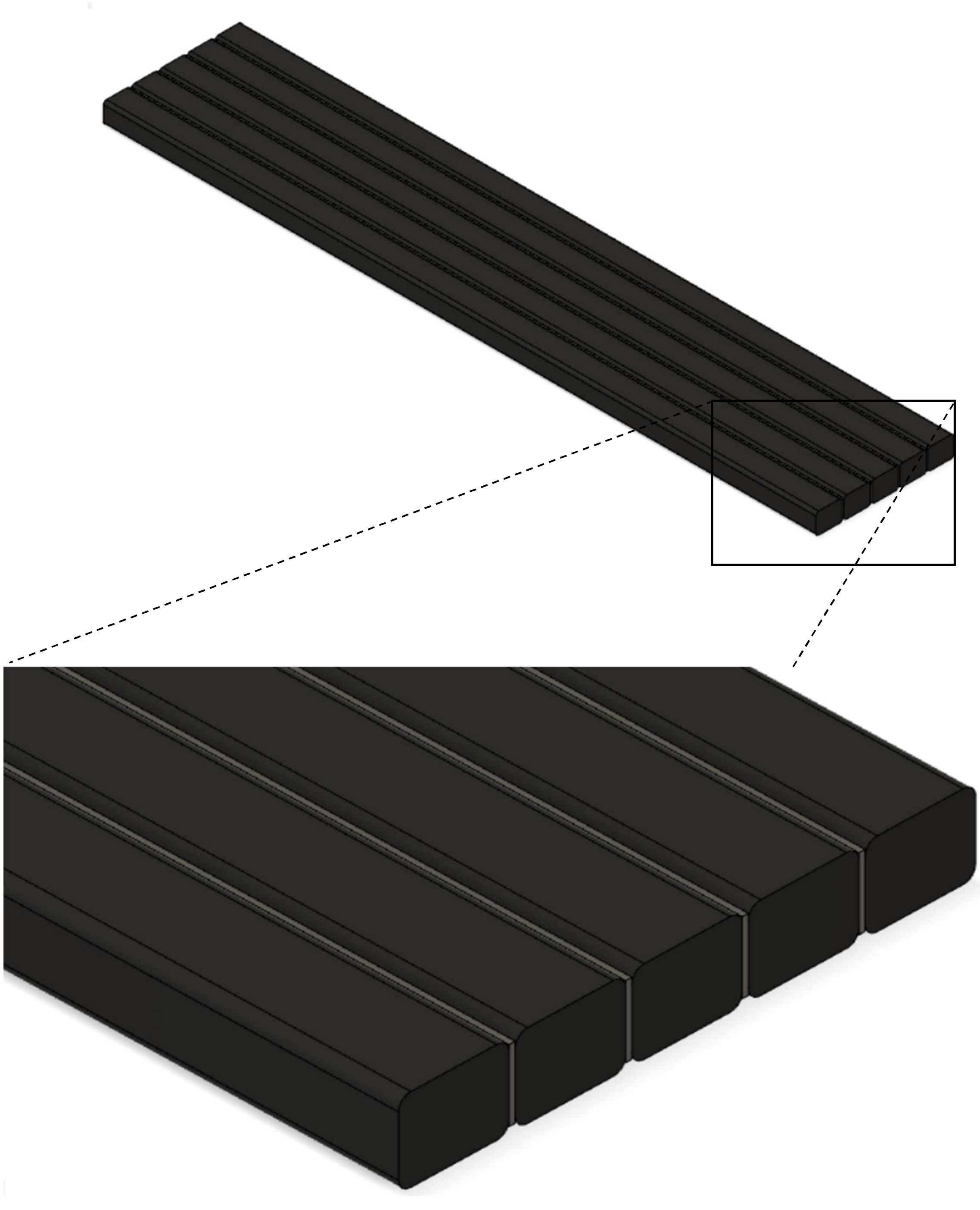

Figure 8 Isometric view, (7x9) x 5 x (4x½) experimental mat configuration

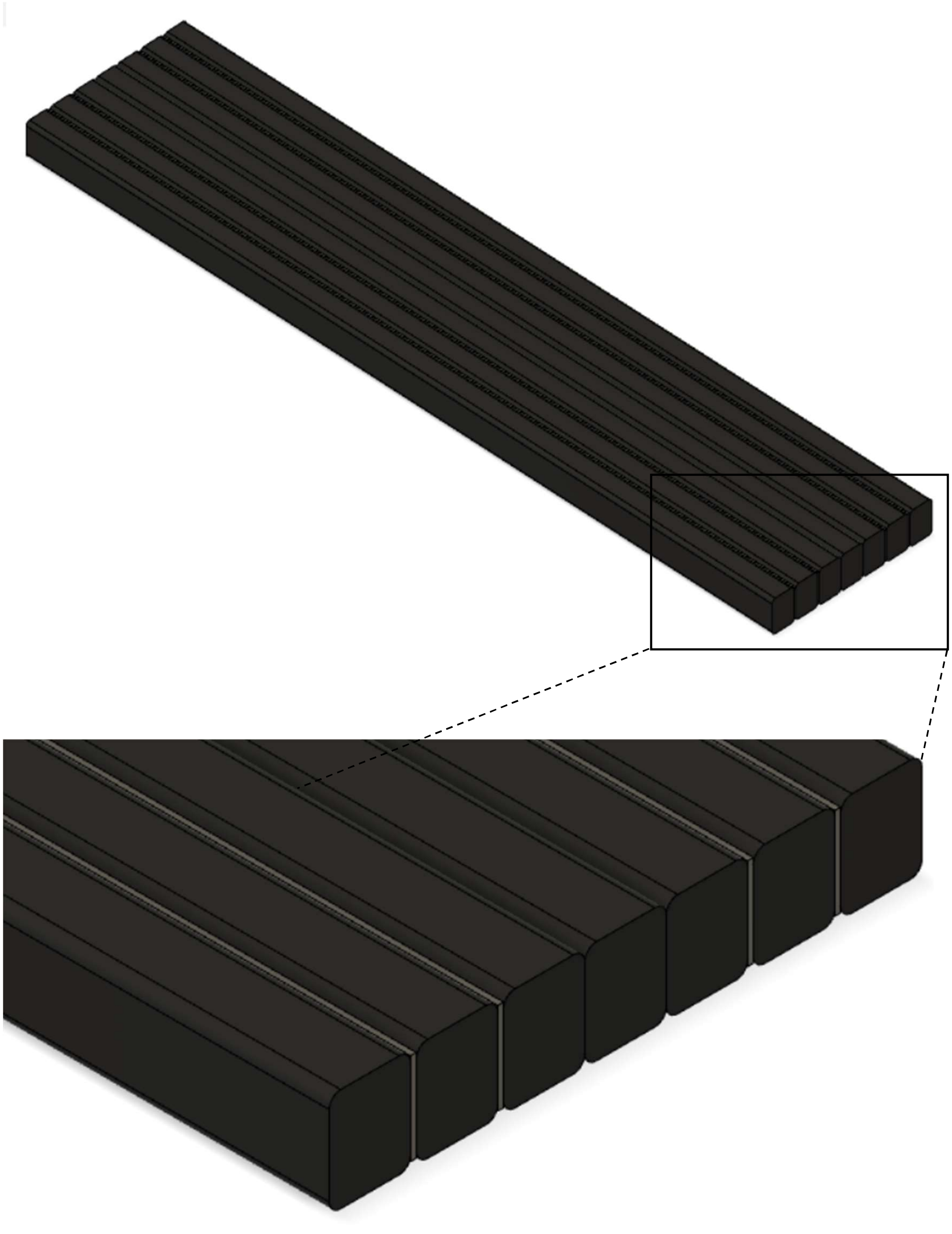

Figure 9 Isometric view, (9x7) x 7 x (4x½) experimental mat configuration

Figure 10 Cross section view, (9x7) x 7 x (4x½) experimental mat configuration

Regarding the testing procedure, the total span for each useable test, i.e. the distance between the two bottom supports of the test frame, was 120 inches. The distance between the load platens was 36 inches. Force was measured directly from the load cell and displacements were measured via two string pot sensors, one located at the center of each outermost beam in the mat, as can be seen in Figure 5 above. A slight variation in each sensor reading was accounted for by taking the average between the two, and using that as the final experimental displacement for analysis purposes. Values for elastic load and displacement were taken within the linear range of each output load-displacement curve. It should be noted from the data in Table 1 that a total of 17 tests were performed. For model formulation only 13 of those tests were utilized. Configuration (*7x9) x 5 x (NS)* was removed from analysis, resulting in a loss of two data sets. Configuration (*7x9) x 5 x (NS)* was subjected to adaptations of the testing procedure that resulted in unusable data. Specifically, the original total span in the 4-point load frame was 180 inches but after the stroke limit of the testing frame's actuator was reached during the first tests, the total span length was decreased to 120 inches as detailed above, and used for the rest of the specimens. The other two data sets that were removed from the total original population of 17 were tests that underwent procedural error present during testing, resulting in error in the collected results. Table 2 presents the key results of the 13 useable data sets. As a final note pertaining to both (*NS)* configurations, due to the lack of steel flitch plates in the mat structures, the material behavior cannot be considered linear elastic. Both exhibited viscoelastic material behavior, and thus the time-dependent rate of loading would also have to be taken into account. As such, configuration (*9x7) x 7 x (NS)* is included in the presented results, but was only used for ancillary analysis and comparison, which is discussed in further detail in the next sub-section. Lastly, note the asterisk and value of the average experimental stiffness for the *(9x7) x 7 x (4x½)* configuration. For that configuration the highest stiffness value was used, instead of averaging the values across all tests. This was done in compensation for procedural error that occurred with the tests of that configuration.

CONFIG.	Test No.	Elastic Force [lbs]	Elastic Disp. [in.]	Exp. Stiffness [lbs/in.]	Average Exp. Stiffness [lbs/in.]	Failure Load [kips]	Average Failure Load [kips]
(9x7) x 7 x (NS)	1	57,650	3.002	19,210	**19,160**	93.68	93.31
	2	57,450	3.005	19,120		92.93	
(7x9) x 5 x (4x¼)	2	35,060	1.159	30,270	**27,860**	88.82	86.99
	3	35,290	1.387	25,450		85.16	
(7x9) x 5 x (4x½)	1	49,920	1.178	42,380	**40,530**	104.69	105.52
	2	50,310	1.245	40,430		101.03	
	3	49,810	1.284	38,800		110.84	
(9x7) x 7 x (6x¼)	1	79,730	1.156	68,970	**67,960**	180.65	170.72
	2	79,810	1.218	65,560		161.44	
	3	79,960	1.153	69,350		170.08	
(9x7) x 7 x (4x½)	2	100,290	1.486	67,490	**80,630***	182.83	180.93
	3	100,140	1.377	72,750		179.03	
	4	100,340	1.245	80,630		196.24	

**see paragraph above for details*

Table 2 Tabulated experimental results

The raw data itself was generated via load-displacement curves for each test, an example of which is presented below in Figure 11 and 12, for the third test of configuration *(9x7) x 7 x (6x¼)*.

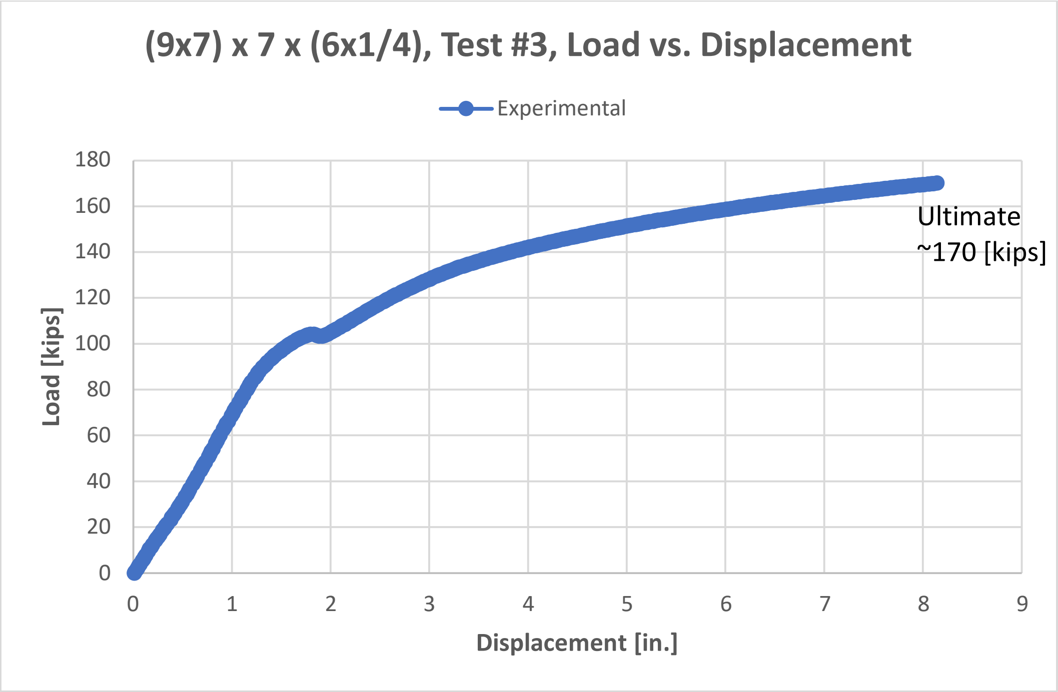

Figure 11 Load vs. Displacement, test #3, configuration (9x7) x 7 x (4x½)

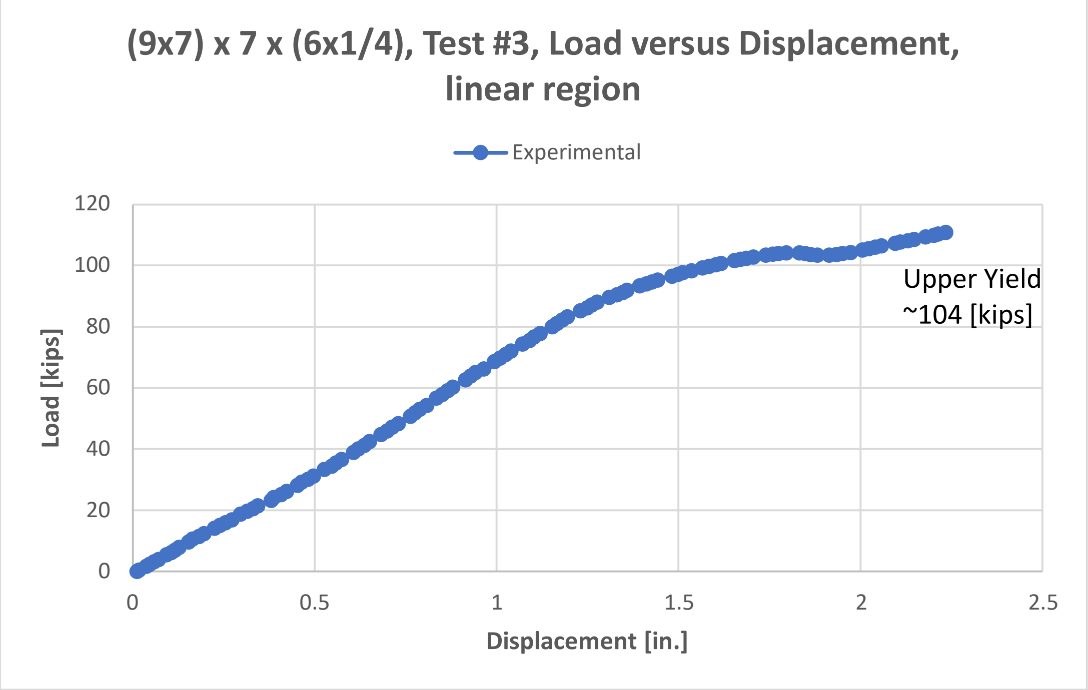

Figure 12 Load vs. Displacement, test #3, configuration (9x7) x 7 x (4x½), linear region only

ANALYTICAL MODEL

The analytical model was based on Euler-Bernoulli beam theory and, to compare to the experimental data, was formulated using conditions and geometry representative of a four-point bend test. The choice of Euler-Bernoulli beam theory for an analytical model was based on the design and material properties of the experimentally tested mats, and the method and procedure of the testing, i.e. the applied loads, geometry and material properties of the experimental specimens. First, given the nature of the expected loading on said mats, and the heterogenous composition of glass fiber-HDPE in conjunction with A36 steel, the assumption and employment of elastic material properties and pertaining theory is valid. Secondly, although the physical geometry of the mats classifies them as plate structures, again the nature of the loading and test procedure, that being a four-point bend test, instead allows for modeling of the mats as a heterogenous beam consisting of discreet regions of homogeneous makeup (Allen and Haisler, 1985). Those discreet regions being the glass fiber-HDPE and A36 steel, respectively. This is valid as elastic plate structures experiencing loading and deformation in one coordinate direction can be represented as elastic beam structures instead, with minimal loss of accuracy and beneficial trade-off of analytical model simplification (Blodgett, 1966). This previous concept also required use of modulus weighted properties within supporting theory and model development, which will be expanded upon further below.

The principal assumptions of Euler-Bernoulli beam theory are: the beam must have relatively small deformation under applied loading, and planar cross-sections of the beam must remain planar, and normal to the deformed axis (Allen and Haisler, 1985). Figures 13 and 14, below, demonstrate these two assumptions.

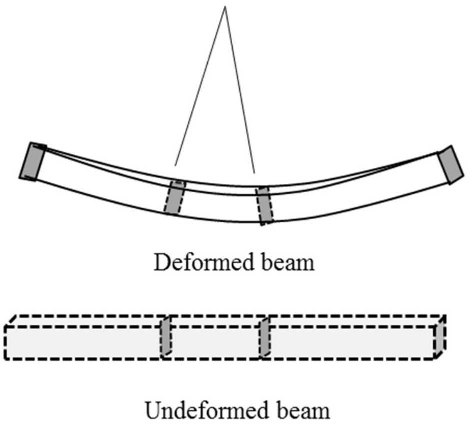

Figure 13 Euler-Bernoulli deformed beam

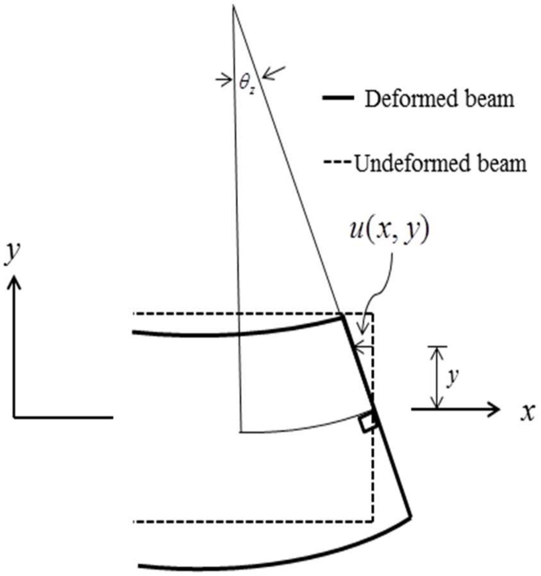

Figure 14 Diagram of Euler-Bernoulli deformed beam

Expanding upon the above assumptions with regards to the above figures, assumption one requires that θ_z and *u(x,y)* in Figure 14 are relatively small. Assumption two is demonstrated in Figure 13, and is present in Figure 14, wherein the solid-lined plane of the deformed beam is marked with a right-angle annotation referenced to the deformed horizontal axis.

Returning to analytical model development, several different configurations were experimentally tested as detailed above, but for purposes of applying analytical theory, necessary parameters will remain in variable form. A representative graphical depiction was created of the above experimental testing. This is presented in Figures 15 and 16 below. Note, the interval for the depiction starts the domain of the beam at the location of the outer support of the test frame, and purposefully excludes the extra portions of the mat on either end, outside the supports. Both those regions non-load bearing and thus were neglected within the analytical model. The coloring and quantity of the beam components in Figure 16 are arbitrary.

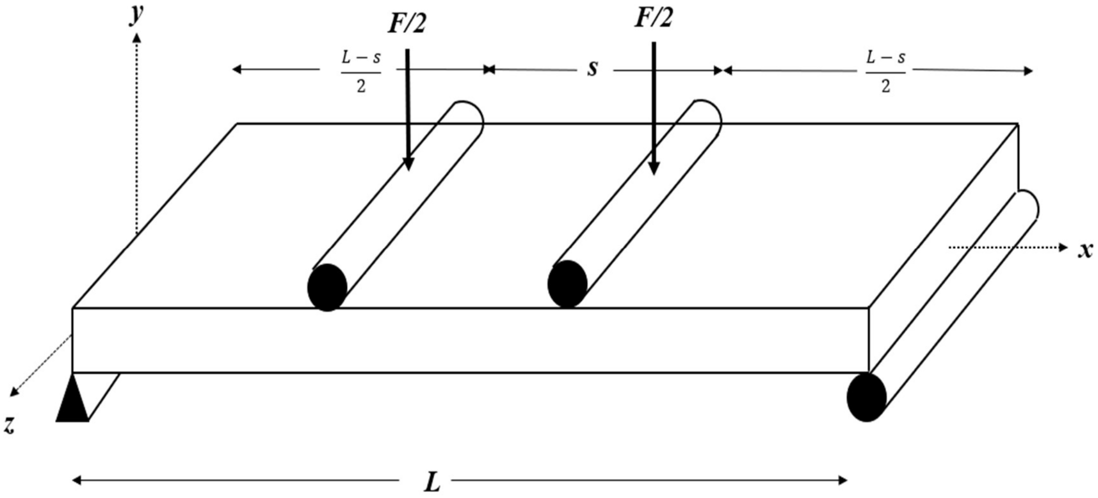

Figure 15 Isometric view, FBD depiction of 4-point bend test

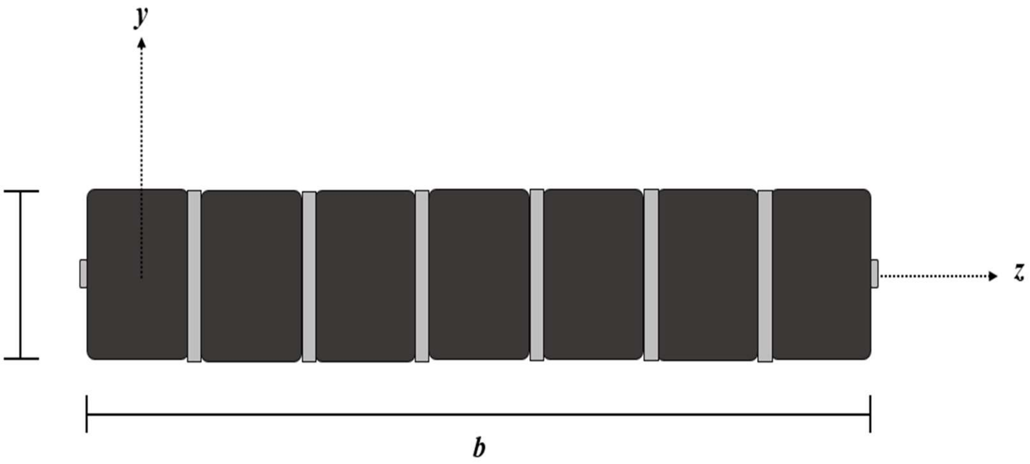

Figure 16 Cross-sectional view, FBD depiction of 4-point bend test

It should be noted with regards to the above depictions that boundary conditions were chosen representative of a simply supported beam. The experimental testing however had two supports limiting y-direction displacement only, and possessed geometry that created a large degree of friction between the supports and the mat during testing. This difference between the analytical model and experimental data is a possible source of error in the model, and had to be addressed again during numerical modeling.

Before continuing, Table 3 is presented below. This table lists all used variables and respective descriptions that will be employed in the remainder of this sub-section. Each variable will remain unitless for simplification of formulation. Table 3 is redundant in nature as all variables will be defined in text, but serves more as a quick reference for the reader.

VARIABLE	**DESCRIPTION**
F	Applied transverse force from 4-point bend test-frame actuator
L	Test length of beam
s	Platen spacing of 4-point bend test-frame
M_z	Internal bending moment about z-axis within beam
v	Displacement component, y-coordinate direction
E_R	Reference Young's modulus, ($Note$: $E_R = E_C$)
E_C	Young's modulus polymer composite plastic beam
E_i	Young's modulus for material at which point equation is applied
y	Centroidal distance and moment arm, y-coordinate direction
n	Number of discreet homogeneous portions of heterogenous beam
I_{zz_i}	Standard area moment of inertia the *ith* homogenous portion of beam
I_{ZZ}^{*}	Modulus weighted area moment of inertia of mat cross-section
c_n	Constant of integration

Table 3 Employed variables and descriptions for sub-section

From the above depictions, shear and bending moment diagrams can be created, which are presented in Figure 17 below.

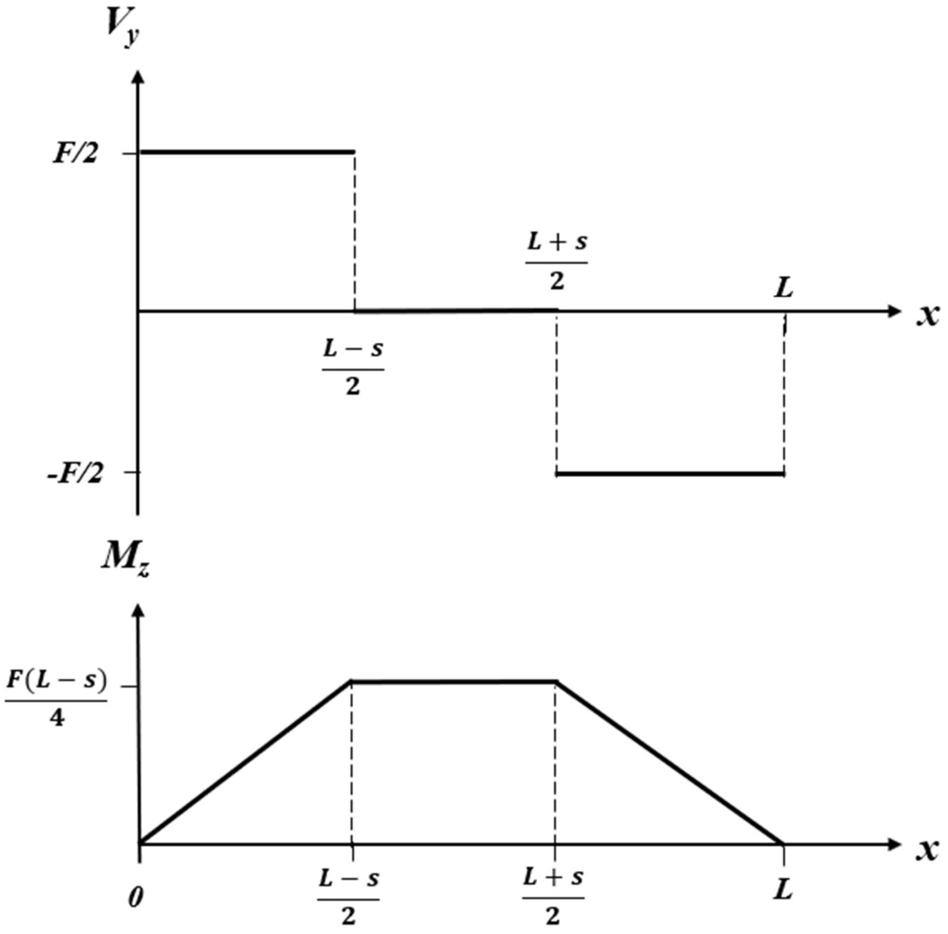

Figure 17 Shear (top) and bending moment (bottom) diagrams of 4-point bend test utilizing Euler-Bernoulli beam theory

Next, the classic Euler-Bernoulli relation of beam deformation to loading, geometry and material properties, is presented below in Eqn. (1), and is already formulated with regards to a heterogeneous beam of discreet homogeneous regions

(Allen and Haisler, 1985). This relation is derived from the governing equations for Euler-Bernoulli pure bending of a beam, which in turn are derived from Newton's First Law. This derivation is not covered here as it is already widely published and available.

$$\frac{d^2v}{dx^2} = \frac{M_z}{E_R I_{zz}^*} \qquad \text{Eqn. (1)}$$

With regards to Eqn. (1) above, M_z is the internal bending moment about the z-axis within the beam, v is the displacement of the beam along the y-axis, E_R is the reference modulus, which in this case is equal to E_C, the modulus of the polymer composite and I_{ZZ}^* the modulus weighted area moment of inertia of the portion of the beam being evaluated.

Before continuing, modulus weighted properties must be discussed for use in formulation of the analytical model. As previously mentioned, a heterogeneous beam made of discreet homogenous portions may have physical and geometric properties calculated via use of a reference modulus, in this case the modulus of the polymer composite, acting as a weighting modulus (Allen and Haisler, 1985). Properties can then be formed in a summation fashion, as is demonstrated below in the calculation of the modulus weighted area moment of inertia of the *ith* portion of the beam cross-section, Eqn. (2).

$$I_{zz}^* = \sum_{i=1}^{n} \frac{E_i}{E_R} I_{zz_i} \qquad \text{Eqn. (2)}$$

In Eqn. (2), n is the number of homogenous portions within the heterogenous beam and I_{zz_i} is the standard area moment of inertia the *ith* homogenous portion and E_i the modulus of the *ith* homogeneous portion of the heterogenous beam. The parallel axis theorem need not be applied here as all discreet regions in the mat shared the same centroidal axis.

Returning to the analytical model formulation, first piecewise intervals were created along the domain of the beam. Due to the symmetry of the beam and loading, only two discreet intervals were needed. Utilizing Figs. (3b.8) above, the acting moments were determined for each interval in variable form. Substituting the intervals and their respective moments into Eqn. (1) creates the piecewise Eqns. (3) below:

$$E_c I_{zz}^* \frac{d^2 v}{dx^2} = \begin{cases} \frac{F}{2} x, & 0 \le x \le \frac{L-s}{2} \\ \frac{F}{2}\left(\frac{L-s}{2}\right), & \frac{L-s}{2} \le x \le \frac{L+s}{2} \end{cases} \qquad \text{Eqn. (3)}$$

Taking Eqn. (3), double integration was performed on each interval, creating four unique constants of integration. This process is represented by Eqns. (4) and (5) below.

$$E_c I_{zz}^* \frac{dv}{dx} = \begin{cases} \frac{F}{2}\frac{x^2}{2} + c_1, & 0 \le x \le \frac{L-s}{2} \\ \frac{F}{2}\left(\frac{L-s}{2}\right) x + c_2, & \frac{L-s}{2} \le x \le \frac{L+s}{2} \end{cases} \qquad \text{Eqn. (4)}$$

$$E_c I_{zz}^* v(x) = \begin{cases} \frac{F}{2}\frac{x^3}{6} + c_1 x + c_3, & 0 \le x \le \frac{L-s}{2} \\ \frac{F}{2}\left(\frac{L-s}{2}\right)\frac{x^2}{2} + c_2 x + c_4, & \frac{L-s}{2} \le x \le \frac{L+s}{2} \end{cases} \qquad \text{Eqn. (5)}$$

Next, the constants of integration were determined. First the essential condition represented by Eqn. (6) was applied to Eqn. (5) to solve for constant c_3.

$$v(x = 0) = 0 \qquad \text{Eqn. (6)}$$

$$c_3 = 0 \qquad \text{Eqn. (7)}$$

Second, the essential condition represented by Eqn. (8) was applied to Eqn. (4) to solve for constant c_2.

$$\frac{dv}{dx}(x = L/2) = 0 \qquad \text{Eqn. (8)}$$

$$c_2 = -\frac{F}{2}\left(\frac{L-s}{2}\right)\left(\frac{L}{2}\right) \qquad \text{Eqn. (9)}$$

Next, two different matching conditions were applied, both at the location of the left platen, i.e. the platen closest to the coordinate system origin, where one of the symmetrically applied point loads was located. Those two conditions are:

$$\frac{dv}{dx}\left(x \rightarrow \frac{L-s}{2}\right) = \frac{dv}{dx}\left(x \leftarrow \frac{L-s}{2}\right) \qquad \text{Eqn. (10)}$$

$$v\left(x \rightarrow \frac{L-s}{2}\right) = v\left(x \leftarrow \frac{L-s}{2}\right) \qquad \text{Eqn. (11)}$$

Utilizing Eqns. (4), (9) and (10), constant c_1 was resolved:

$$c_1 = \frac{F}{4}\left(\frac{L-s}{2}\right)^2 - \frac{F}{2}\left(\frac{L-s}{2}\right)\left(\frac{L}{2}\right) \qquad \text{Eqn. (12)}$$

Utilizing Eqns. (5), (7), (9), (11) and (12), constant c_4 was resolved:

$$c_4 = \frac{F}{12}\left(\frac{L-s}{2}\right)^3 \qquad \text{Eqn. (13)}$$

Next, the exact Euler-Bernoulli solution of the deflection of the beam within each domain interval was determined, Eqn. (14) is representative of the second domain interval solution, where the point of interest was located.

$$v(x) = \frac{1}{E_c I_{zz}^*}\left[\frac{F}{4}\left(\frac{L-s}{2}\right)x^2 - \frac{F}{2}\left(\frac{L-s}{2}\right)\left(\frac{L}{2}\right)x + \frac{F}{12}\left(\frac{L-s}{2}\right)^3\right],$$

$$\frac{L-s}{2} \leq x \leq \frac{L+s}{2} \qquad \text{Eqn. (14)}$$

Displacements of the experimental mat tests were measured via two sensors, one located at the mid-span of each outermost beam component in the mat, as detailed previously. This now becomes the point of interest within the domain of our free-body diagrams presented above. In variable form this point is *x(L/2)*. Plugging in the point of interest of the domain into Eqn. (14) resulted in Eqn. (15), representing the final analytical model representative of the experimental testing presented previously. Note in Eqn. (15), *F* represents the total force applied by the frame.

$$v(x = \frac{L}{2}) = \frac{F}{E_c I_{zz}^*}\left[\frac{1}{4}\left(\frac{L-s}{2}\right)\left(\frac{L}{2}\right)^2 - \frac{1}{2}\left(\frac{L-s}{2}\right)\left(\frac{L}{2}\right)\left(\frac{L}{2}\right) + \frac{1}{12}\left(\frac{L-s}{2}\right)^3\right] \qquad \text{Eqn. (15)}$$

Rearranging terms, Eqn. (15) becomes:

$$v(x = \frac{L}{2}) = \frac{F}{E_c I_{zz}^*}\left[-\frac{1}{4}\left(\frac{L-s}{2}\right)\left(\frac{L}{2}\right)^2 + \frac{1}{12}\left(\frac{L-s}{2}\right)^3\right] \qquad \text{Eqn. (16)}$$

Plugging in 120 inches for L and 36 inches for s, i.e. the geometry representative of the experimental testing presented above, and rearranging terms to isolate F/v on the LHS, the final analytical model of the structure's stiffness, S_{th} is as follows:

$$\frac{F}{v(x=\frac{L}{2})} = S_{th}\left(\frac{L}{2}\right) = E_c I_{zz}^{*}\,[-31626]^{-1} \qquad \text{Eqn. (17)}$$

The above mat stiffness analytical formulation was chosen for direct comparison to experimental results, and later, numerical results. Note the negative value formed from the test geometry constant due to the chosen coordinate system used in the free body diagrams above. Next, correlation of the analytical model was carried out.

Correlation of the analytical model was performed via comparison of the experimental data to respective calculated values from the analytical model. Specifically, the construction mat stiffness, or applied force over correlating displacement, was used. Below in Table 4 are the tabulated results comparing the experimental mat configuration stiffnesses to analogous stiffnesses calculated via the Euler-Bernoulli analytical model. Note the calculated modulus weighted properties for each mat configuration, formed as detailed above.

Reference Modulus/Polymer Composite Modulus, $E_c = 203{,}500\ psi$					
CONFIGURATION	$I_{zz}^{*}\ [in^4]$	**Flexural Rigidity, $E_c I_{zz}^{*}\ [lbs * in^2]$**	**Avg. Exp. Stiffness, $S_{exp,avg}\ [^{lbs}/_{in}]$**	**Theoretical Stiffness, $S_{th}\ [^{lbs}/_{in}]$**	**Percent Difference [%]**
(9x7) x 7 x (NS)	2,977	605,769,000	19,160	19,150	0.05
(7x9) x 5 x (4x¼)	3,851	783,752,000	27,860	24,780	12.41
(7x9) x 5 x (4x½)	6,416	1,305,752,000	40,530	41,290	1.83
(9x7) x 7 x (6x¼)	12,097	2,461,769,000	67,960	77,840	12.69
(9x7) x 7 x (4x½)	15,137	3,080,435,000	80,630	97,400	17.22

Table 4 Tabulated data, experimental mat stiffnesses and correlating analytical stiffness

A graphical correlation between the experimental data and analytical model is presented in Figure 18 below.

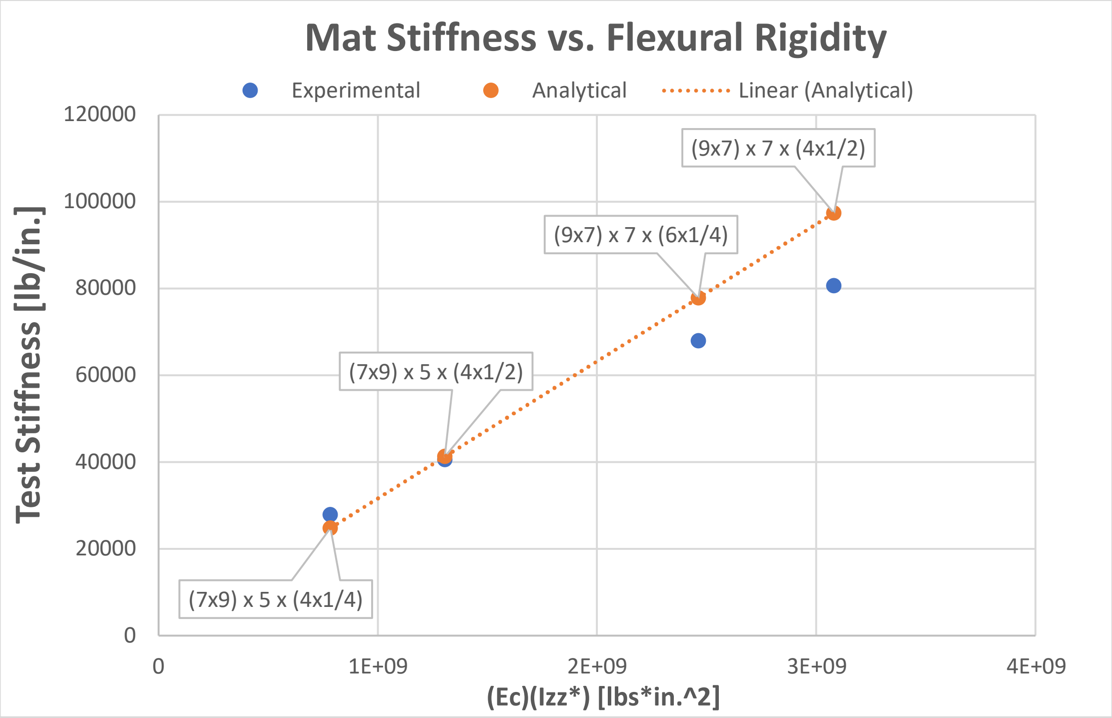

Figure 18 Analytical model correlation, experimental and analytical mat stiffness comparison

As can be seen from Figure 18 the analytical model compared reasonably well to the experimental data. Variation between results can be attributed to the difference between the analytical model and experimental procedure. Specifically, first, the analytical model used a simply supported boundary conditions for the beam, with one pinned-end and one roller-end. In reality, the supports of the test, pictured in Figure 5 above, were both roller-type supports, but with a degree of friction between the support and mat structure. The friction generated at the supports during experimental testing would be the first source of variation between the results. The second source regards the mechanical fastening method of the beam components in the mat. The analytical model assumed the beam components that form the mat to be fully bonded, i.e. the curvature of all beam components in the mat, during deformation, is the same. In reality, and in the experimental testing, a degree of partial interaction occurs between the beam components. This partial interaction is the second source of variation between the results. The phenomena of partial interaction between beam components will be addressed again, and covered in more detail, in the Optimization section. A third source of variation was the assumed elastic behavior of the polymer campsite material, in reality the material is viscoelastic.

Before continuing, detail must be provided on the reference modulus value presented and used above in Table 4. That value was calculated as an effective modulus of the glass fiber-HDPE material, utilizing the *(9x7) x 7 x (NS)* configuration results and the formulated analytical model. Although present in the data in the previous section and this one, the *(9x7) x 7 x (NS)* configuration was only used to form the effective modulus value, which was used as the modulus of the polymer composite throughout this thesis. Use of a calculated effective modulus stems from applicable theory regarding functionally graded materials (Miyamoto, 1999). Use of that theory was necessary as the internal structure of the polymer composite beam changes from a hard-outer shell layer to a more porous-soft core. Figure 19 depicts a cross-section of a polymer composite beam, and highlights the phenomena referenced above.

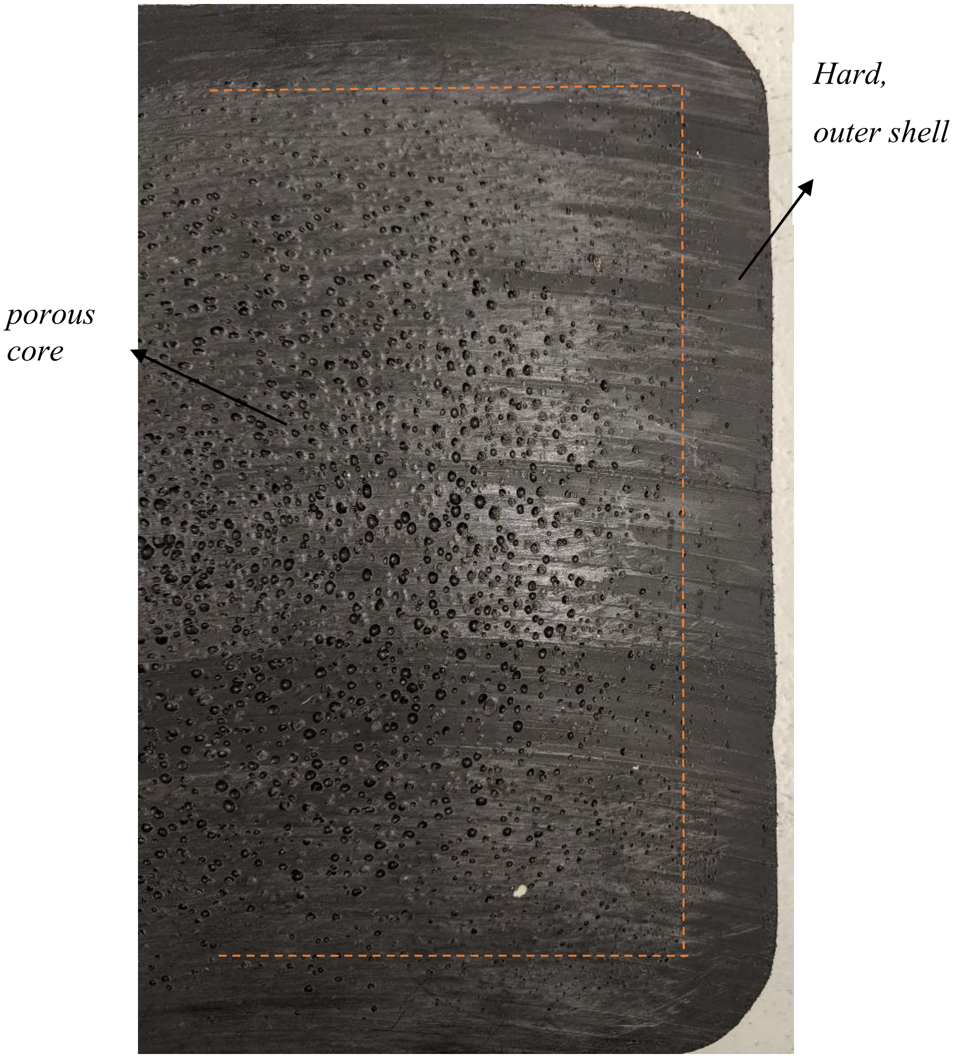

Figure 19 Physical cross section of polymer composite beam

With the analytical model established, numerical models were then generated to create another point of comparison for modeling methodology purposes.

NUMERICAL MODELING

The next step in modeling methodology was to generate numerical finite element models representative of the experimental testing completed, to provide another point of comparison against the experimental results and the analytical model. Three-dimensional numerical models were created in the commercially available ANSYS program. These models were generated utilizing the same geometry, material properties, and boundary conditions employed in the experimental testing.

Regarding the numerical boundary conditions employed, constant force was applied along lines representative of the imprint of the test frame platens, each line assigned half the total applied load. For supports, two cylindrical rigid-body, ground-fixed supports were modeled and employed. These supports were used to create a convex, frictionless contact region against the mat, and provide the necessary essential boundary conditions for the numerical model. Each mat configuration that contained secondary beam components was modeled. The (*9x7) x 7 x (NS)* configuration, having served the purpose of ancillary calculation of material effective modulus as detailed above, was not modeled numerically. Contact surfaces between beam components were defined as fully bonded, thus no fastening hardware or partial interaction was included in the numerical models (*ANSYS Contact Technology Guide,2004)*. All models used quadratic shape functions and quadrilateral or tetrahedron elements with two-inch side lengths. Both regions of each mat outside the support locations were neglected within the analytical model, but were included in the numerical model, for confirmation of their negligible effect. Vertical displacement of the midspan was used for comparison to experimental and analytical results. Table 5 below is the key tabulated parameters and results of each numerical model. Figures 20 – 28 provide visualization, and more detailed results, of each configuration.

CONFIGURATION	**Nodes**	**Elements**	**Total applied force [lbf]**	**Vertical midspan displacement [in.] (y-direction)**	**Mat stiffness [lbf/in.]**
(7x9) x 5 x (4x¼)	127,280	21,870	35,200	1.5242	23,094
(7x9) x 5 x (4x½)	116,236	20,214	50,000	1.3293	37,614
(9x7) x 7 x (6x¼)	192,240	32,617	79,800	1.1923	66,929
(9x7) x 7 x (4x½)	141,040	37,395	100,260	1.1901	84,245

Table 5 Tabulated numerical model results

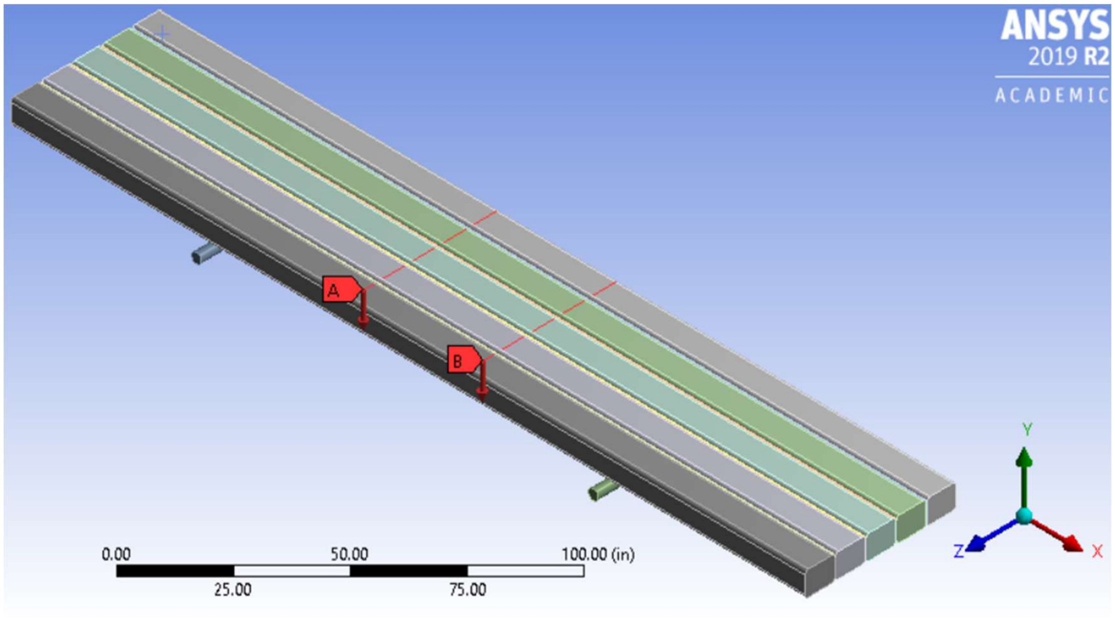

Figure 20 (7x9) x 5 x (4x¼) Configuration CAD model, isometric view

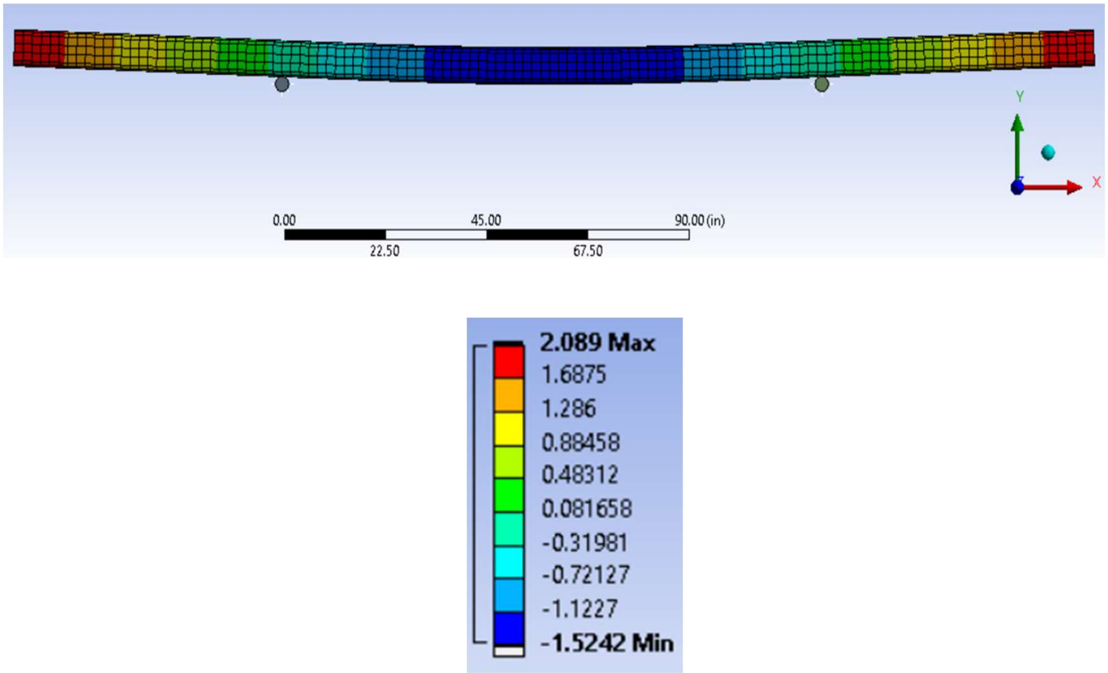

Figure 21 (7x9) x 5 x (4x¼) Configuration numerical model, vertical displacement, [in.]

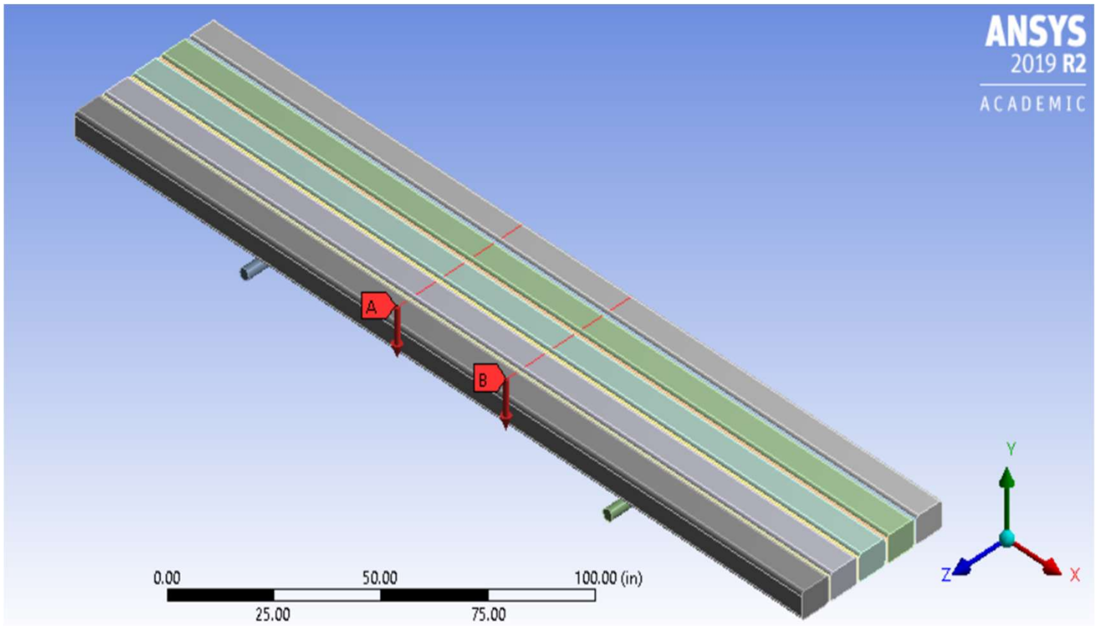

Figure 22 (7x9) x 5 x (4x½) Configuration CAD model, isometric view

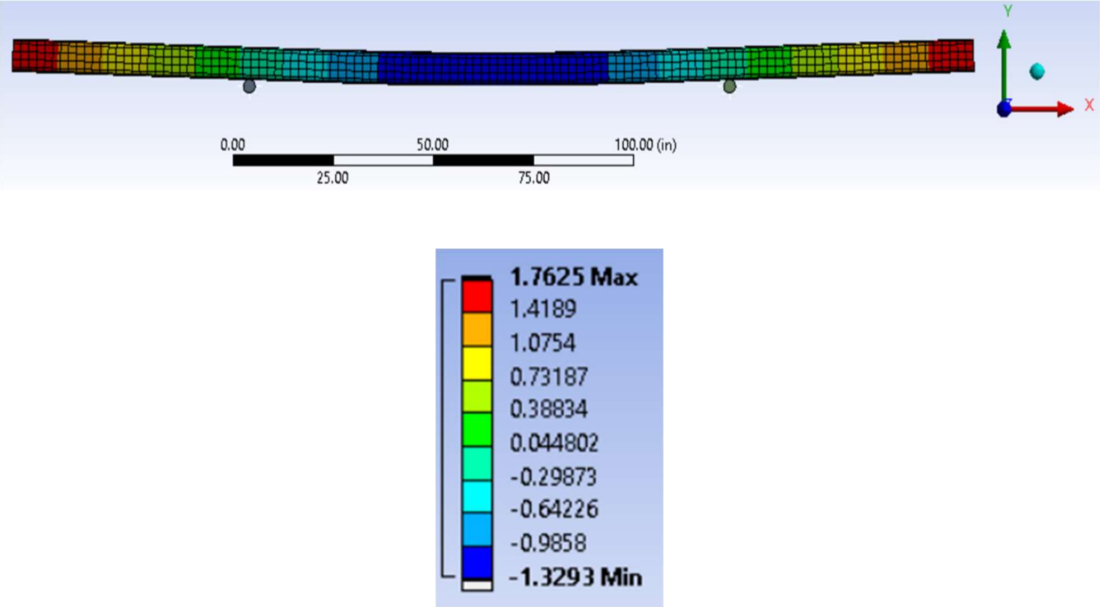

Figure 23 (7x9) x 5 x (4x½) Configuration numerical model, vertical displacement, [in.]

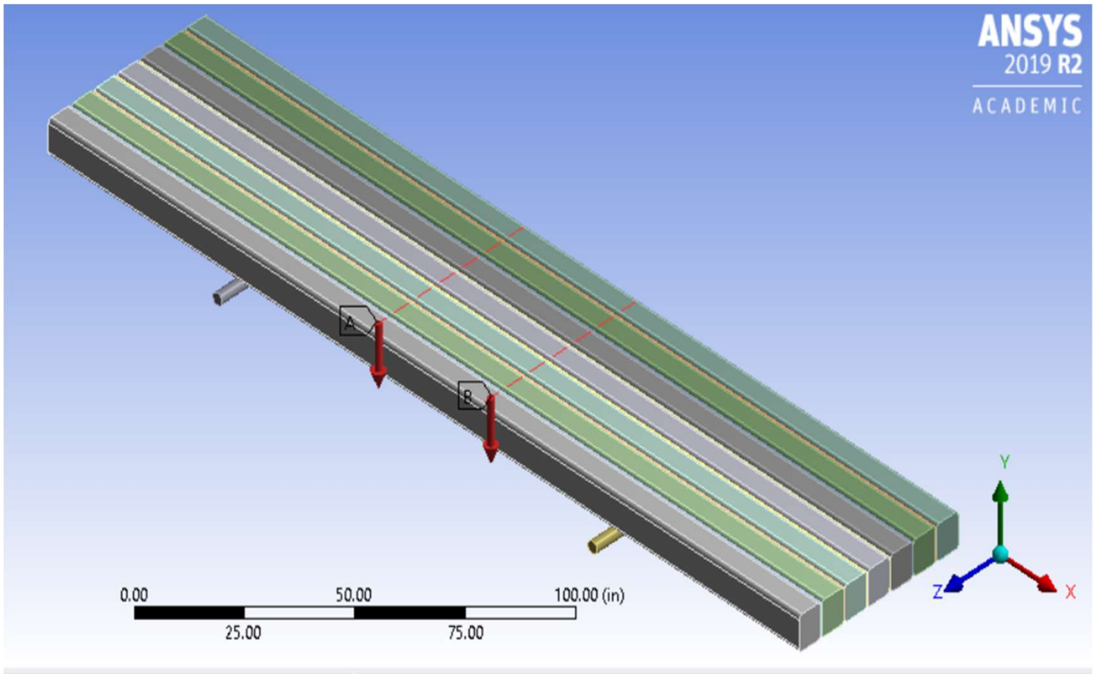

Figure 24 (9x7) x 7 x (6x¼) Configuration CAD model, isometric view

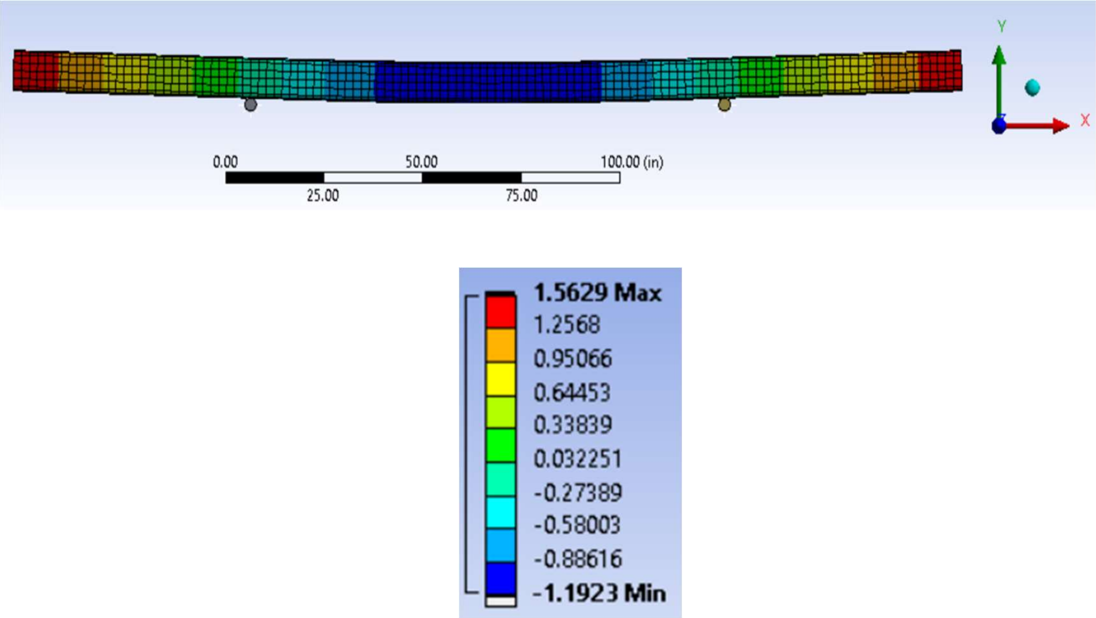

Figure 25 (9x7) x 7 x (6x¼) Configuration numerical model, vertical displacement, [in.]

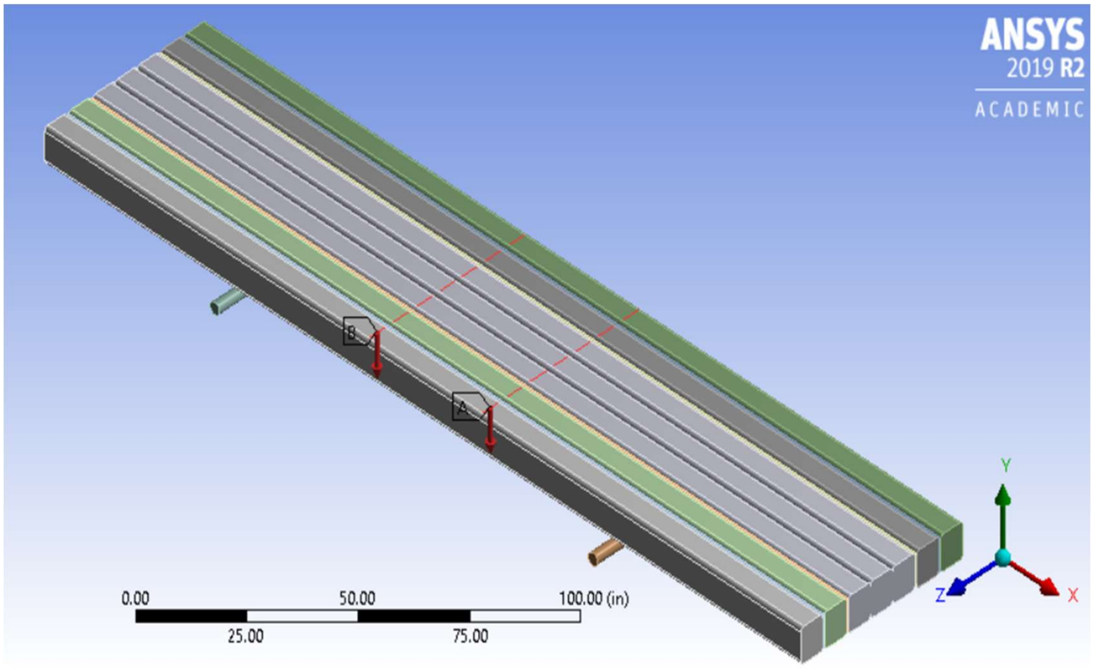

Figure 26 (9x7) x 7 x (4x½) Configuration CAD model, isometric view

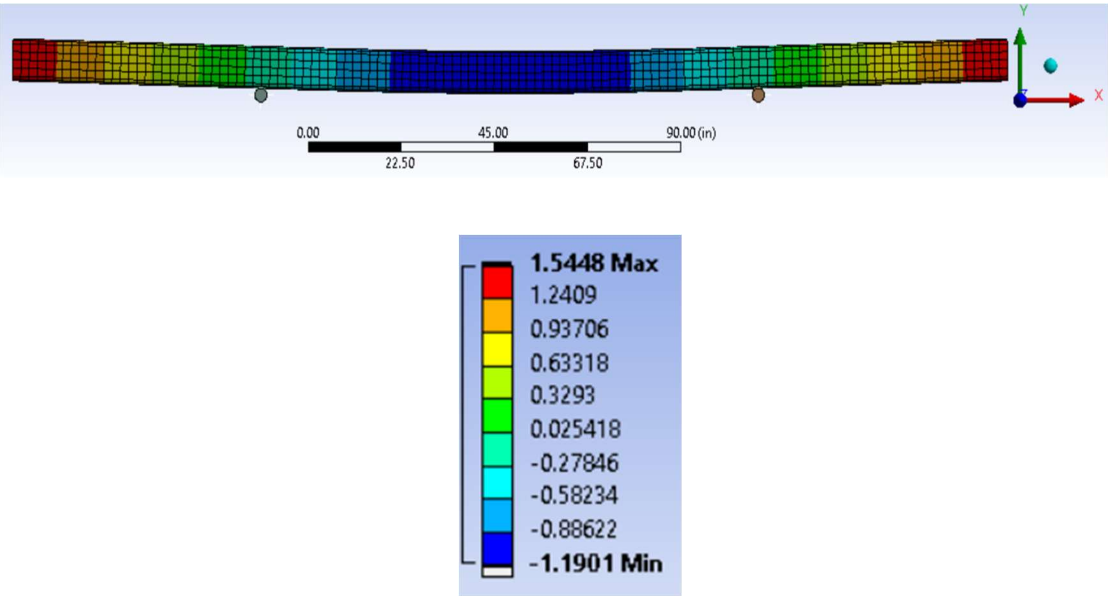

Figure 27 (9x7) x 7 x (4x½) Configuration numerical model, vertical displacement, [in.]

The numerical modeling results were then graphed similar to Figure 18, seen below in Figure 28.

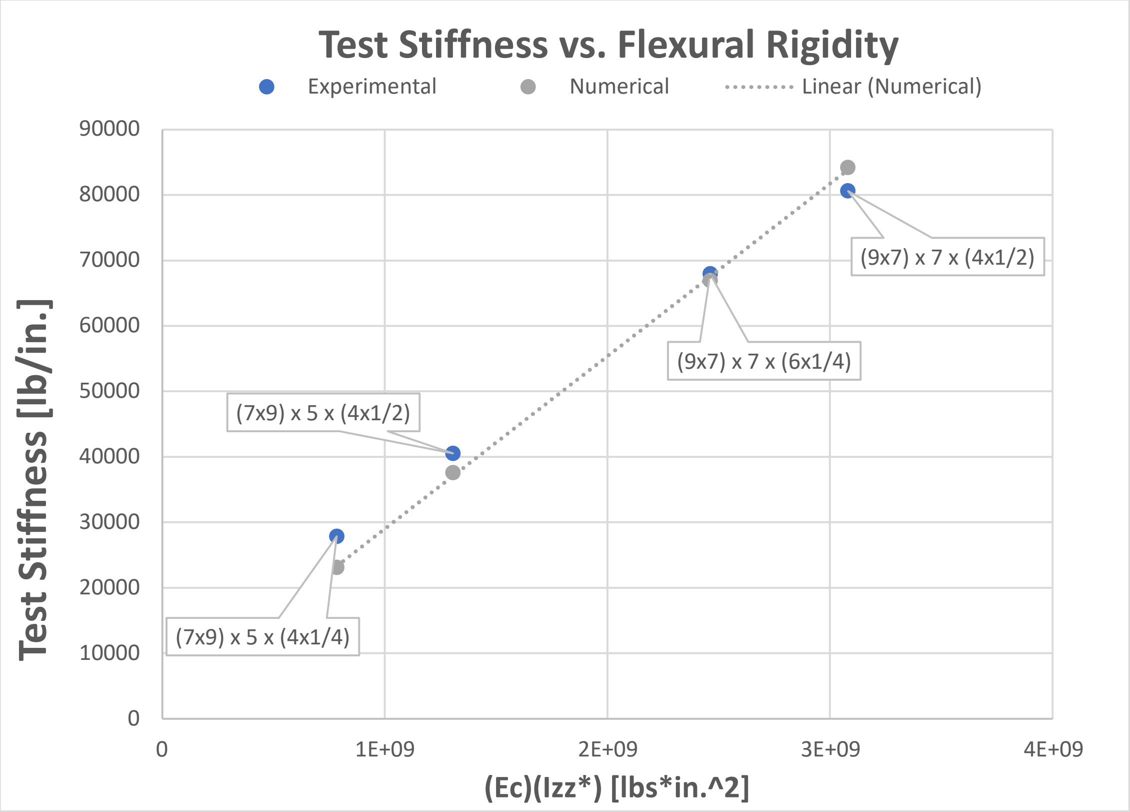

Figure 28 Numerical models correlation, experimental and numerical mat stiffness comparison

As can be seen, the numerical modeling efforts show good correlation with the experimental results. Differences can be attributed to the support conditions and interaction of beam components. Specifically, the rigid-body, ground-fixed, frictionless cylindrical supports used in the numerical modeling once again do not accurately reflect the experimental testing support conditions. The fully-bonded contact regions between beam components also diverge from the conditions within the experimental testing.

MODELING VALIDATION

The last step in the modeling methodology was to compare the different modeling components for validation. This is represented in Table 6 and Figure 29, below. Both include amalgamations of data from the previous three sub-sections. Note that the (*9x7) x 7 x (NS)* configuration is completely absent, as discussed previously.

CONFIGURATION	**Experimental Mat Stiffness [lbs/in.]**	**Analytical Mat Stiffness [lbs/in.]**	**Numerical Mat Stiffness [lbs/in.]**
(7x9) x 5 x (4x¼)	27,858	24,782	23,094
(7x9) x 5 x (4x½)	40,533	41,287	37,614
(9x7) x 7 x (6x¼)	67,960	77,840	66,929
(9x7) x 7 x (4x½)	80,630	97,402	84,245

Table 6 Modeling validation, tabular results

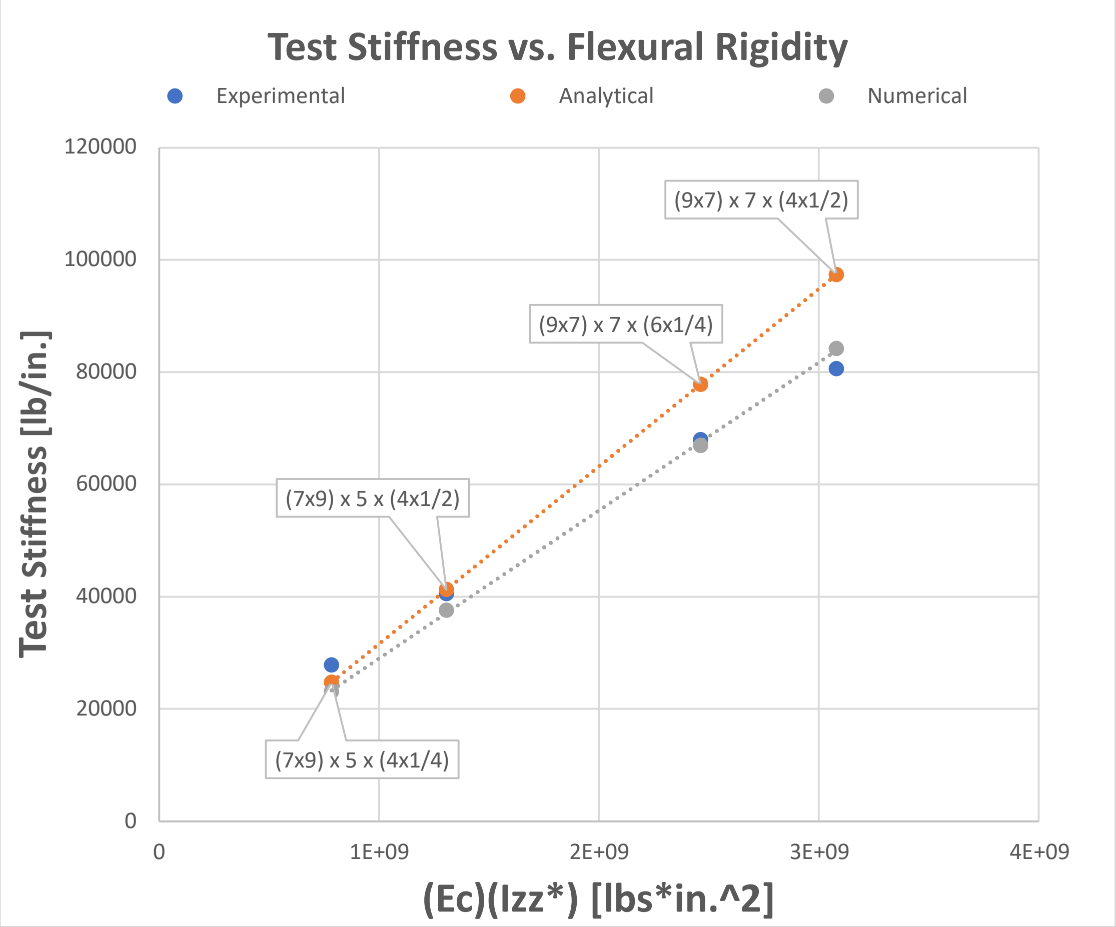

Figure 29 Modeling validation, graphical results, Mat Stiffness vs. Mat Flexural Rigidity

With the above comparison completed, the analytical and numerical modeling efforts were then adapted into predictive tools, and used for the purpose of optimizing the general polymer composite-steel construction mat design.

OPTIMIZATION

Optimization efforts focused on employing the models described in the previous sections, to manipulate the geometry of local components within the mat structures. Optimizations sought to maximize structural strength and minimize material costs. Considering the design of any engineered structure, constraints and parameters fall into three encompassing categories: loads, geometry and material properties. For purposes of this analysis, loads were set to control values to allow for comparison of optimized designs, more detail will be provided below. Material properties of the structure were also constrained as a control, being glass fiber-HDPE polymer composite and A36 structural steel. Geometry, i.e. the number, placement and dimension of components in the structure, encompassed the bulk of optimization efforts. As a last note, this section serves as a general guideline for how this structure should be optimized and analyzed, as such it does not represent a perfect and complete analysis, but instead a guideline for improving the mat design.

PROPOSED INITIAL DESIGN

To begin optimization efforts, some initial constraints and parameters were established. Two major constraints, besides the use of material properties detailed above, were established from the experimental tested designs. First, the primary beam components within optimization efforts were kept constant, representative of the primary beam components within the experimental test mats. These beams, as detailed in the previous sections, are made of a glass fiber-HDPE blend and have a constant prismatic cross section of seven and 1/16 inches by eight and 15/16 inches (7.0625”x8.9375”) with a one-inch radius on all corners. This choice was made for economic purposes; The primary beam components were originally manufactured as a multi-purpose structural component, and due to manufacturing economics, the use of those as the primary beam components served as a design constraint. Second, is the method of fastening of the beam components together into a rigid plate structure. The fastening method for the experimental tested mats was mechanical, as mentioned previously, utilizing specialized nut and bolt hardware. For the given length of the structure at 240 inches, mechanical fasteners with one-inch diameters were used (the actual mounting holes in the structure were tolerance slightly above one inch and were oval in shape, both to allow for ease of installation of the fastening hardware, but for ease of representation in the designs to follow, the mounting hardware holes are all denoted as one inch in diameter). The locations of the fastening hardware began six inches in from either end of the beam, with a uniform spacing of approximately 33 inches. Depictions of example primary and secondary beam components are presented below in Figures 30 and 31. This constraint provided established locations of fastening hardware within the structure for the given length.

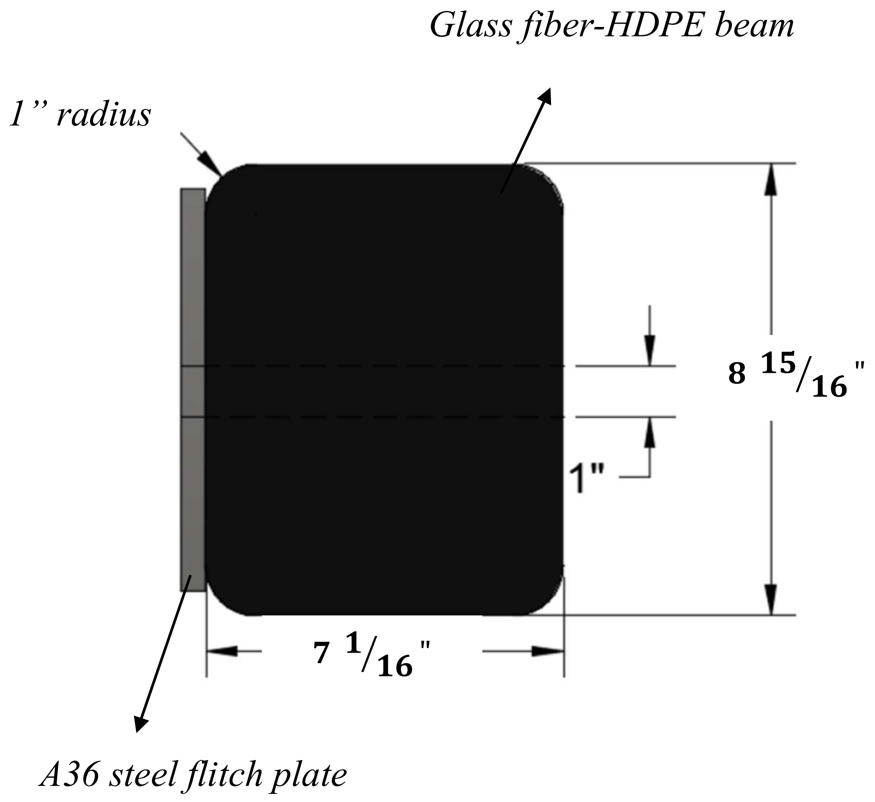

Figure 30 Cross-section view, primary and secondary beam components, unoptimized design

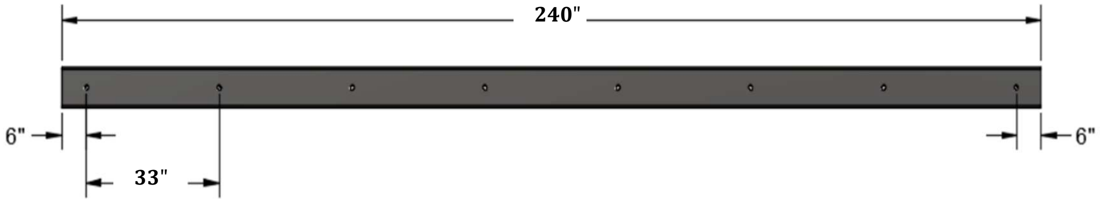

Figure 31 Side view, fastening hardware design constraint

To expand, the method of fastening of the beam components together into a rigid plate structure is determined by the degree of interaction between the beam components.

Optimal fastening is achieved by ensuring full interaction (or at least close enough to assume negligible partial interaction effects) between beam components, while applying the least amount of fastening hardware for economic reasons. For purposes of this thesis, that hardware and its implementation in the structure remained as established by the above design constraint. In other words, the fastening hardware was assumed to be sufficient and creating full interaction between components within the structure as long as the above design constraint was satisfied. In support of that decision, a literature review was performed into partial interaction of composite beam structures. References (5) through (8) and (10) through (11) in the citations section represent that literature review. The summary of that review concluded that from the loading and geometry of the given structure, the dominating partial interaction occurs in the transverse direction, with longitudinal partial interaction having minimal impact. The dominating transverse partial interaction is determined by the difference in curvature between beam components under pure bending. From the experimental data and results, it was determined that while effects of partial interaction between beam components in the structure were present, they were also negligible for modeling and optimization purposes as long as the above constraint was satisfied.

With the above constraints considered, the majority of optimization efforts were then encompassed by the design and implementation of the secondary beam components, the steel flitch plates. To review, unoptimized secondary beam components were implemented as basic prismatic flitch plates, with height *h*, constant thickness *t*. This unoptimized design is presented below in Figures 32 and 33.

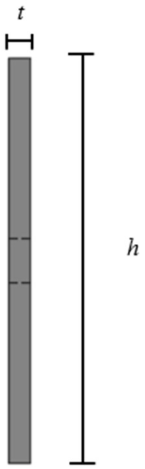

Figure 32 Cross-section view, unoptimized secondary beam component

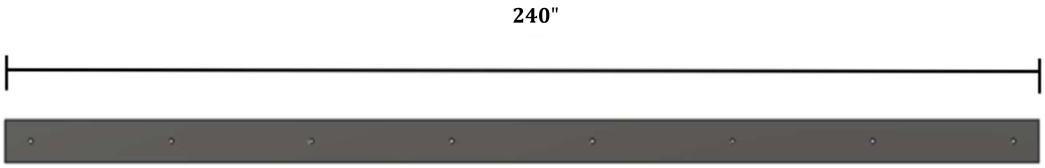

Figure 33 Side view, unoptimized secondary beam component

Conceptual optimized designs were wide ranging, with consideration given to minimized-mass plates, to I-beam and built-up girder type designs. As an example, a conceptual built-up girder design is presented. This built-up girder consisted of steel angle components to form both flanges, and connecting plates in the locations of the fastening hardware to serve as the web. This design is classic structural optimization, changing the geometry of the component to increase the structural properties. A graphical depiction of the conceptual built-up girder design is presented below in several views. Note, the only dimensions present in the depictions are representative of the fastening hardware locations as discussed above, no other dimensions are included as the depictions serve conceptual purposes only. Figure 34 is the side view of the built-up girder, Figure 35 the cross-section view, and Figures 36 an isometric view.

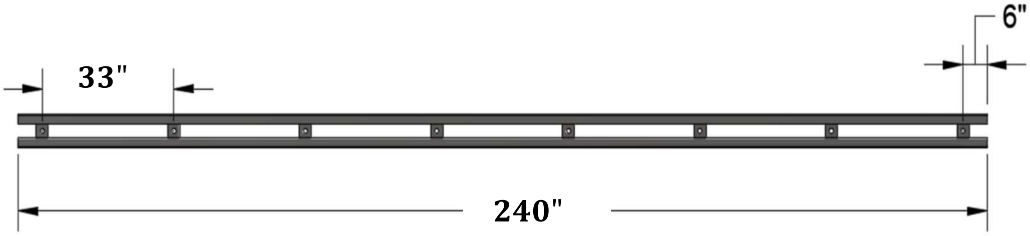

Figure 34 Side view, conceptual secondary beam component design, built-up girder

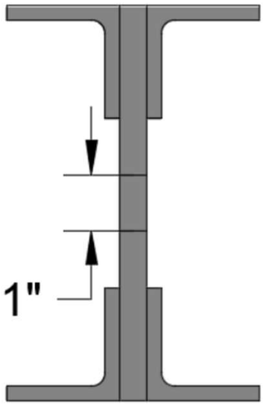

Figure 35 Cross-section view, conceptual secondary beam component design, built-up girder

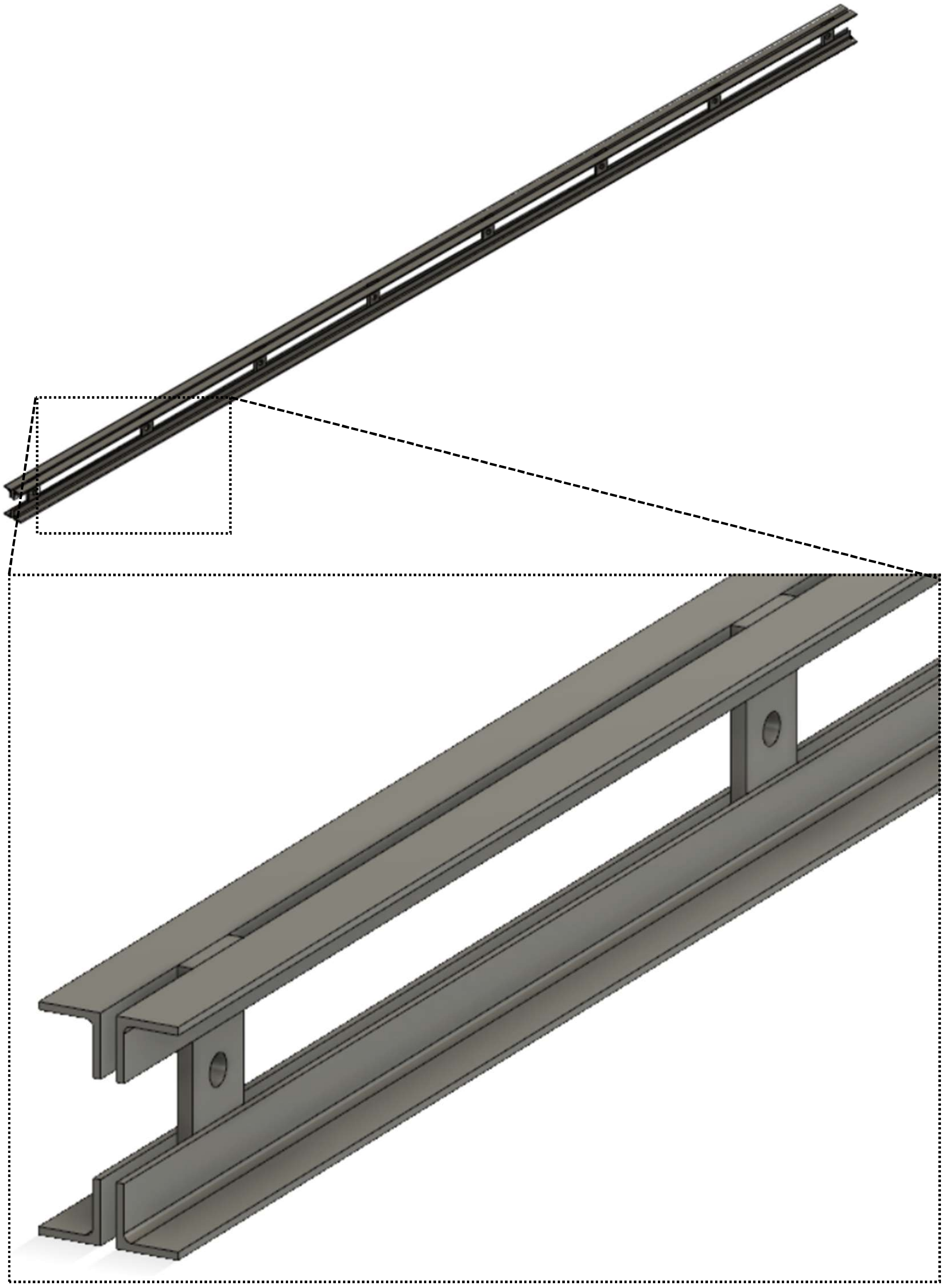

Figure 36 Isometric view, conceptual secondary beam component design, built-up girder

Due to purposes of this thesis being to establish a procedure for modeling and optimization, only one secondary beam component design was chosen for analysis and establishment of process. It should be emphasized however that the overall process established could be applied to any desired secondary beam component design, including both geometry and material property manipulation. The design used is presented below, and represents an I-beam type design. Figure 37 is a side view, Figure 38 a cross-section view and Figure 39 an isometric view. All units are in inches.

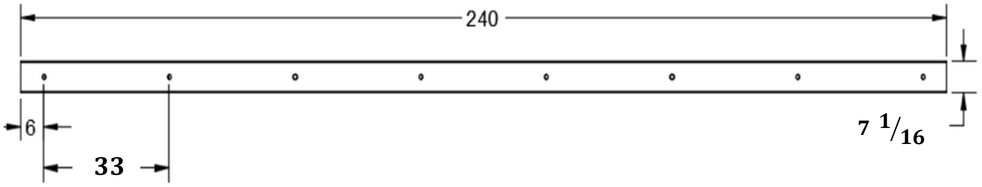

Figure 37 Side view, proposed secondary beam component design

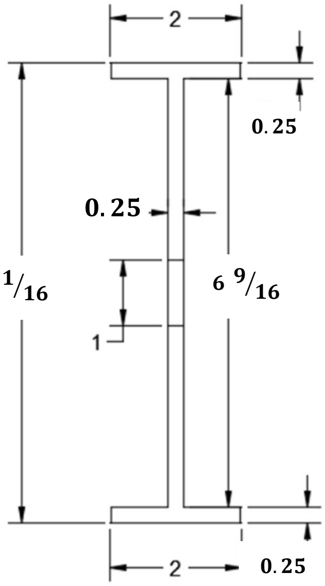

Figure 38 Cross-section view, proposed secondary beam component design

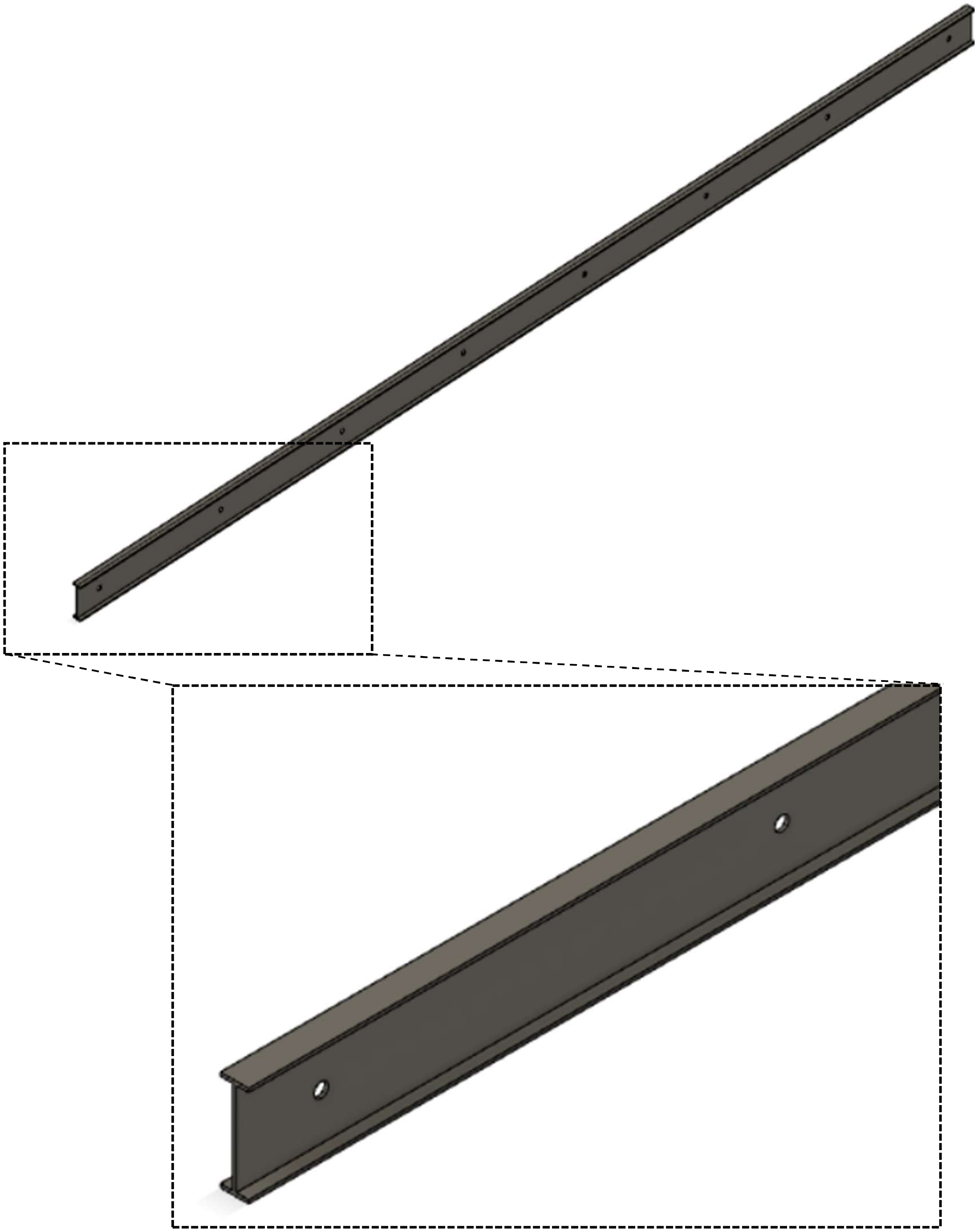

Figure 39 Isometric view, proposed secondary beam component design

Again, the above proposed design served as a starting point to detail the optimization process, to follow in the next section. It should be noted from the dimensions in the figures above that this process was applied to composite beams in the *(7x9)* orientation, and due to the height of the web, would also require the composite beams to be slightly modified with a ¼" inch radius on top and bottom to accommodate the flange. This was utilized in order to accommodate operational usage of the mat itself. The flange should not protrude from the operational-side surface of the mat, as the protruding steel flange would induce excessive wear on any treaded equipment maneuvering on top of it. As such the resulting mating of the above proposed design, and the modified composite beam, appeared as depicted in the cross-sectional view in Figure 40, below.

Figure 40 Cross-section view, mat with proposed secondary beam component

OPTIMIZATION OF SECONDARY BEAM COMPONENTS

Optimization of the secondary beam components, or more broadly the optimization procedure itself, was carried out in three phases. The first phase employed use of another numerical modeling tool, a two-dimensional, linear-elastic finite element frame code, that employed beam-type elements. The second phase, returned to use of

ANSYS for a three-dimensional stress analysis of a single secondary beam component for a localized analysis. Finally, the third and last phase, utilized ANSYS again to implement the secondary beam component back into the overall mat structure, and perform a global three-dimensional stress analysis.

The first phase of optimization efforts utilized an open source 2-D, linear-elastic finite element frame code, written in the Python 3 programming language. This tool was established for the optimization procedure, as it served to quickly evaluate structural strength of single secondary beam components, without having to do more time intensive 3-D modeling. With this tool, a wide range of designs could be quickly implemented and evaluated, allowing for a narrowing-down of designs before moving into more complex 3-D modeling. Standard modeling conditions were set up for use in the frame code numerical model. This included geometry and boundary conditions. First, modeling geometry was set up to represent the same conditions as the experimental four-point bend tests. Applied total force was set to a fixed amount at 2,000 pounds force, applied as two, 1,000-pound force point loads. For geometric properties, an area moment of inertia value was calculated using Figure 38 above, and Eqn. (18) below. Eqn. (18) utilizes summation of individual area moment of inertias in conjunction with parallel axis theorem.

$$I_{zz} = 2\left(\frac{bh^3}{12} + Ad^2\right)_{flange} + \left(\frac{bh^3}{12}\right)_{web} \qquad \text{Eqn. (18)}$$

An input file was then generated for the secondary beam component, comprised of seven nodes and six elements. Figure 41 below depicts a nodal map representative of the single proposed secondary beam component.

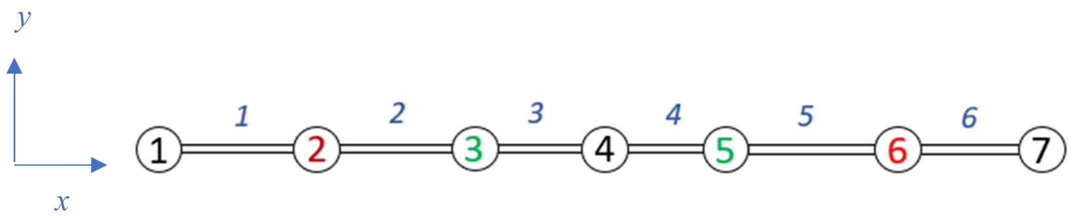

Figure 41 Nodal map, frame code numerical model, proposed secondary beam component design

Figure 42 below shows a graphical representation, for visualization purposes only, of the Python frame code input and output. Note, axis values are in inches.

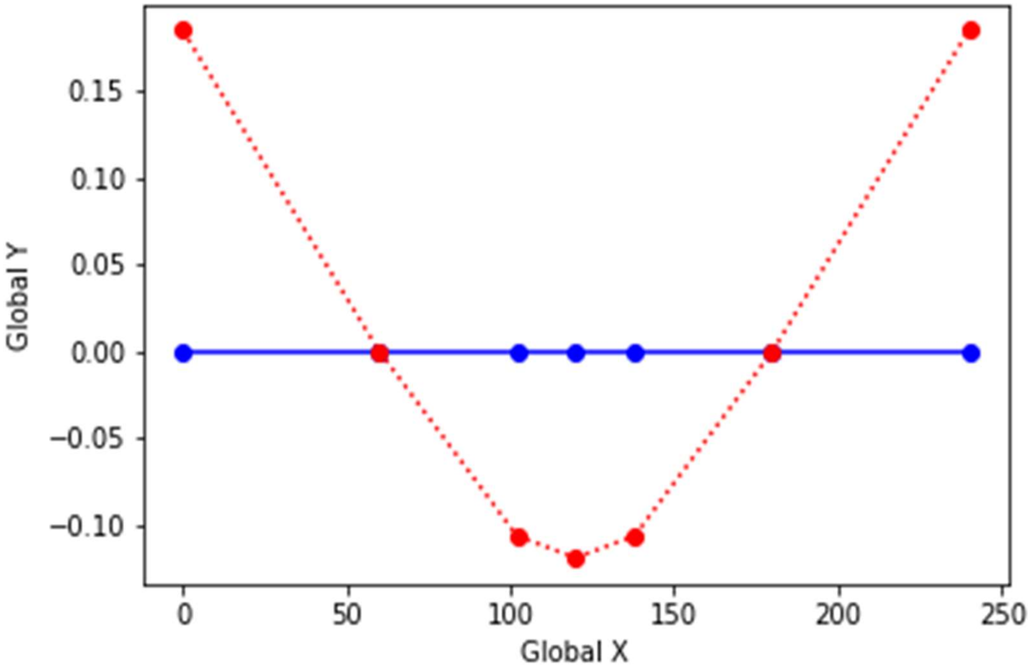

Figure 42 Frame code numerical model graphic input/output, proposed secondary beam component design, units in inches

Results were compared to the analytical Euler-Bernoulli beam theory model established previously, utilizing material properties and geometry of the single secondary beam component design, and results were an almost perfect match, with negligible variation stemming from computing round-off error. Similar analysis was done for the unoptimized secondary beam components, those being the *(7x9)* orientation steel flitch plate, both ½” and ¼” thick. Total mass for each secondary beam component was calculated and Figure 43 below was generated, comparing the single secondary beam component stiffness with total applied load of 2,000 pounds force, to the total component mass.

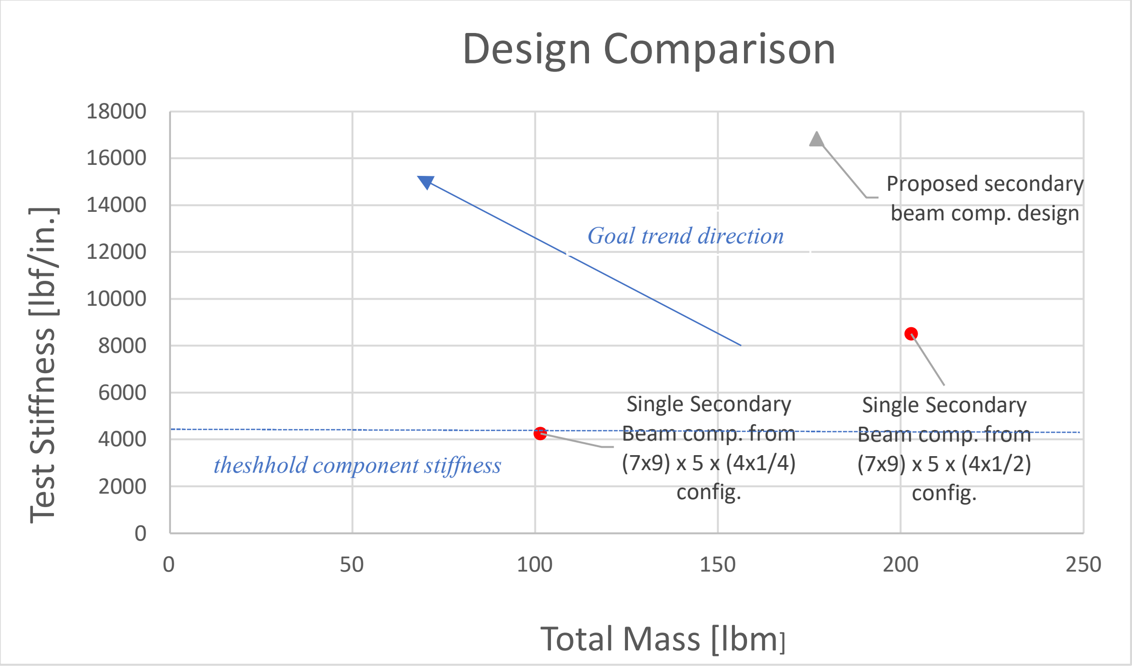

Figure 43 Phase one optimization, secondary beam component design comparison

As can be seen from the figure above, the total mass of the proposed secondary beam component design has significantly less material mass than the ½” unoptimized flitch plate, yet has much greater structural test stiffness than either the ¼” or ½” plate. Utilizing current market prices for A36 plate steel, material mass can be translated to material cost (*North American Carbon Steel Price Index*, 2019). The proposed secondary beam design cost was approximately 60 USD per unit, compared to approximately 34 USD for the ¼” unoptimized SBC and approximately 69 USD for the ½” unoptimized secondary beam component.

Next, phase two was carried out within the ANSYS finite element program, specifically a three-dimensional stress analysis. Phase two was paramount as phase one, and the above Python frame code, do not account for local stress concentrations and buckling. Specifically, for a structural component such as the proposed secondary beam component design above, shear stress at the junction of the flange and web are a serious concern for component failure, along with buckling of the web itself, both of which would require separate analysis through finite element ANSYS models, or a similar modeling tool with appropriate capabilities. Similar boundary conditions were set up for the ANSYS model as presented in the numerical modeling section, above, however the applied force was changed to 2,000 pounds force to match the phase one modeling efforts. Figure 44 below depicts the ANSYS modeling setup.

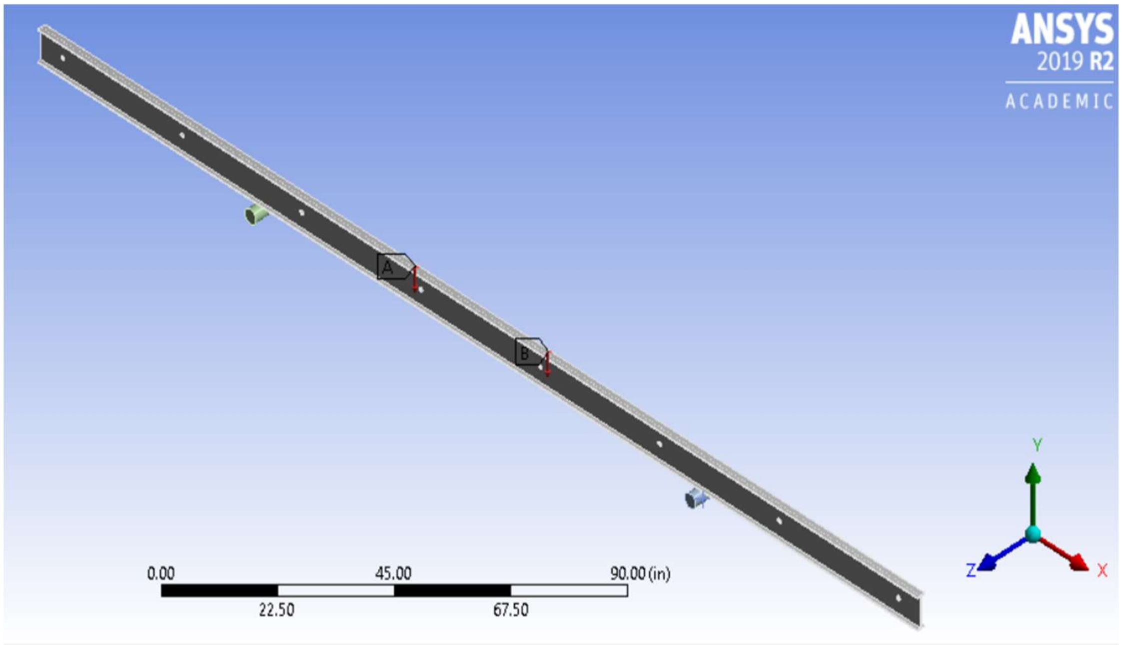

Figure 44 Phase two optimization, proposed secondary beam component CAD model

Directional displacement was predicted in inches, and is depicted by Figure 45 below. The mesh for the approximation totaled 58,900 nodes and 27,836 quadratic elements.

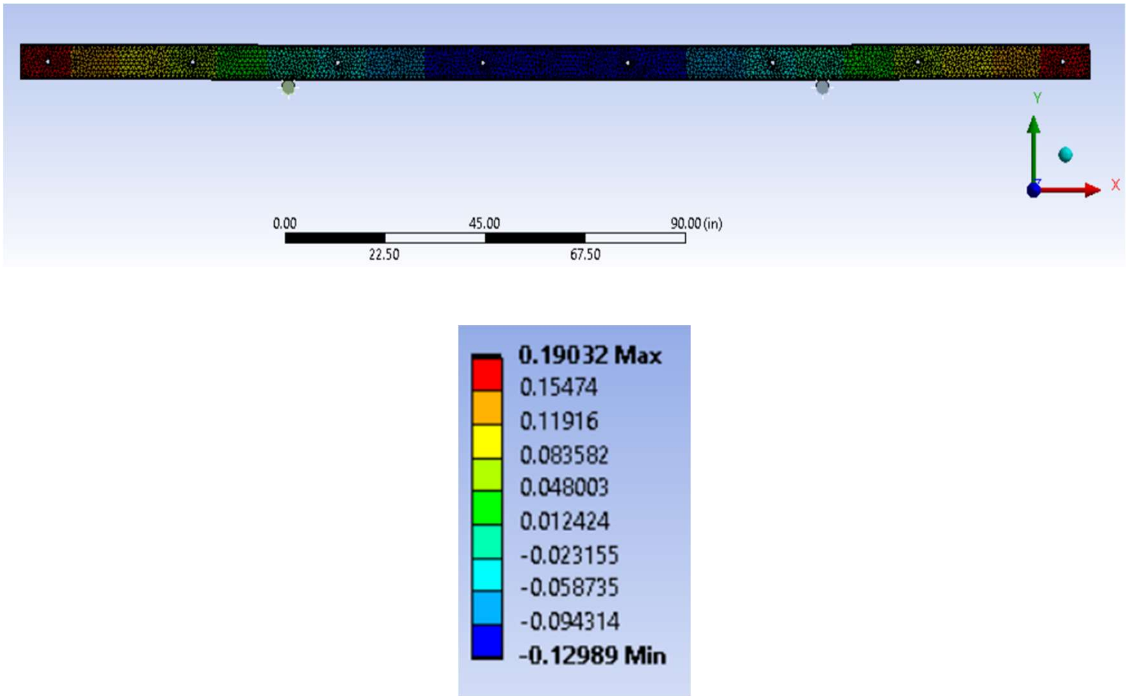

Figure 45 Phase two optimization, proposed secondary beam component numerical model, vertical displacement [in.]

Taking the above midspan displacement approximation of 0.12989 [in.] and dividing 2,000 pounds force by that value, a stiffness approximation of 15,398 [lbf/in.] was determined, which was comparable to the Python frame code value of 16,838 [lbf/in.]. Next the stress approximation was analyzed using the Von Mises yield criterion. This failure criterion was chosen as Von Mises equivalent stresses are a conservative failure analysis for ductile materials, in this case A36 structural steel. Figure 46 below depict the Von Mises stresses approximation of the above model in units of [psi].

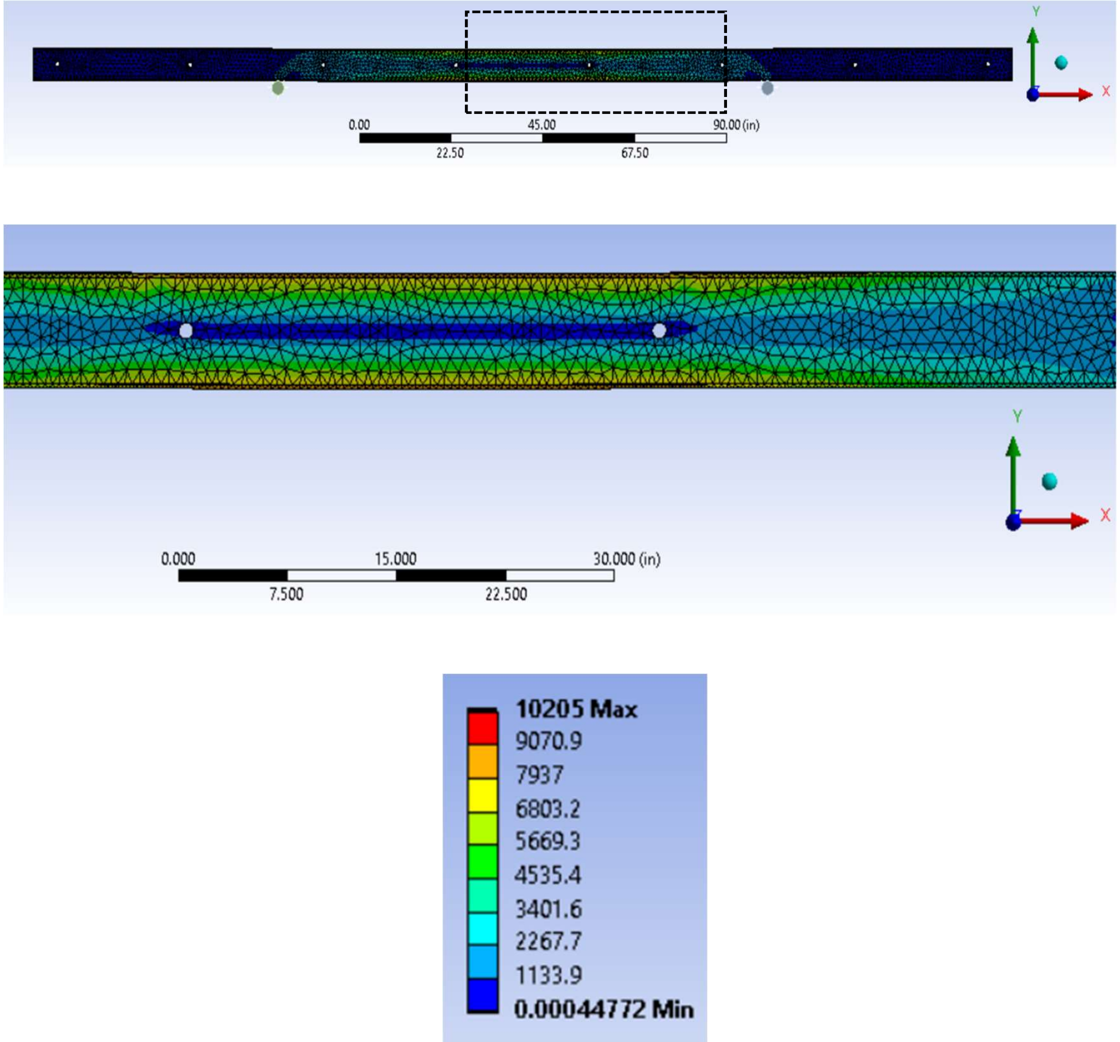

Figure 46 Phase two optimization, proposed secondary beam component numerical model, Von Mises stresses [psi]

As can be seen from the above figure, the maximum approximated Von Mises stresses were 10,205 pounds per square inch, well below the yield point of A36 steel at 36,000 pounds per square inch.

It should be highlighted that this second phase of the optimization analysis was established more as a necessary step in the overall procedure. The main purpose of this step is to emphasize the importance of local analysis of any secondary beam component design. Recommendations for more thorough analysis would include subjecting the model to various loadings, and studying shear stresses and local component buckling, as mentioned at the beginning of this step. This step is especially crucial when evaluating a design similar to the one presented in Figures 34-36 above, to determine possibility of local web failure. With the proposed secondary beam component design above, a full web was implemented and thus the possibility of local web shear failure is less significant. As for buckling, while analysis must be done, implementation of the secondary beam component back into the global structure would significantly decrease the possibility of local web buckling failure as the primary beam components to either side would act in support.

The third and final phase of the optimization procedure was to reincorporate the new secondary beam component design back into the overall mat structure for global analysis and compare it to the previous designs to ensure an optimization was achieved. The mat geometry itself is already presented above in Figures 37-40. That geometry was put into a three-dimensional ANSYS numerical model with the boundary conditions established in the section above. Due to the proposed secondary beam component design being compared to the 7” orientation of both the ¼” and ½” plates, two approximation were carried out. The first with natural boundary conditions comparative to that of the ¼” plate, in configuration *(7x9) x 5 x (4x¼)*, seen in Figures 20-21 and row one of Table 5. The second with natural boundary conditions comparative to that of the ½” plate, in configuration *(7x9) x 5 x (4x½),* seen in Figures 22-23 and row two of Table 5. Figure 47-48 below represent the results of the numerical model, which contained 267,924 nodes and 140,379 quadratic elements.

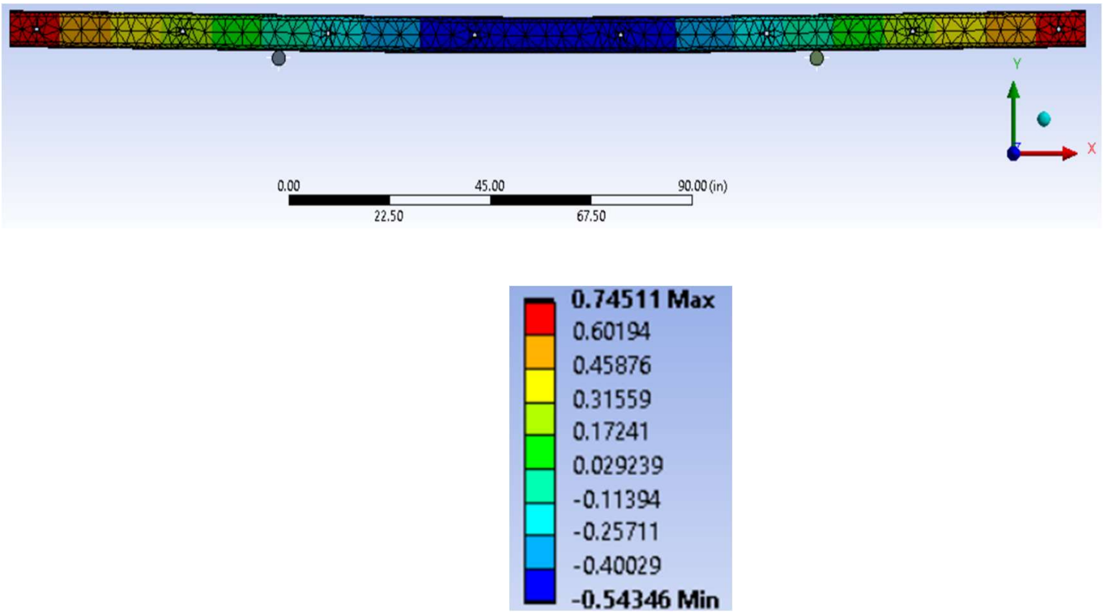

Figure 47 Phase three optimization, global numerical model, midspan displacement [in.], (7x9) x 5 x (4x¼) boundary conditions

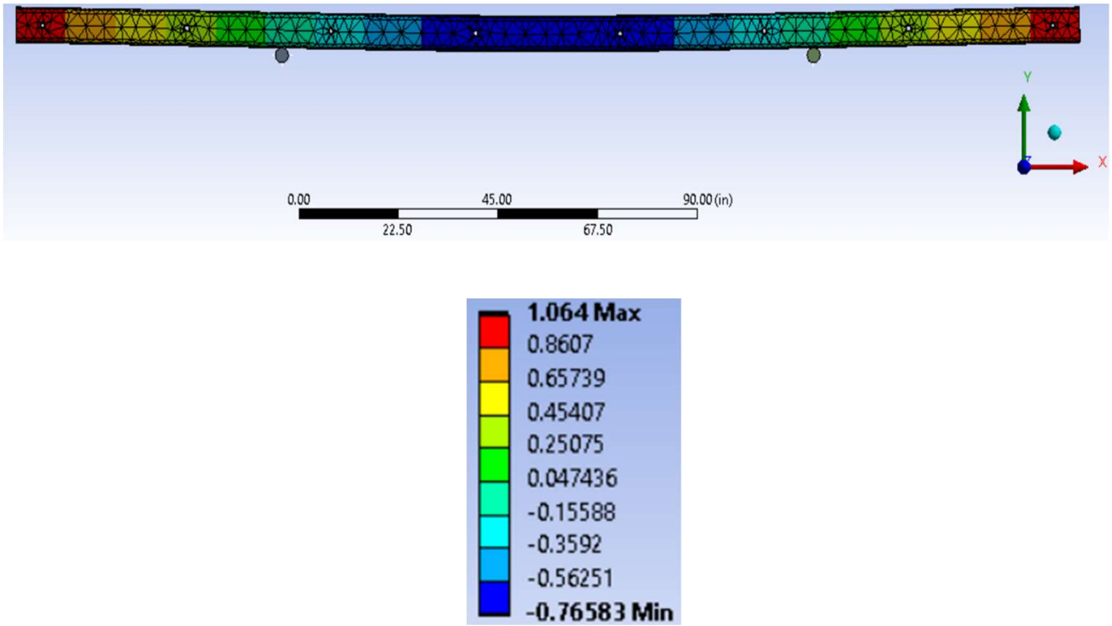

Figure 48 Phase three optimization, global ANSYS numerical model, midspan displacement [in.], (7x9) x 5 x (4x½) boundary conditions

Taking the above results and comparing against appropriate unoptimized designs resulted in Table 7 below.

CONFIG.	**Total applied force in model [lbf]**	**Approx. midspan displacement [in.]**	**Approx. mat stiffness [lbf/in.]**
(7x9) x 5 x (4x¼)	35,200	1.5242	23,094
(7x9) x 5 x (4x½)	50,000	1.3293	37,614
(7x9) x 5 x (4x PSBC)	35,200	0.54346	64,770
(7x9) x 5 x (4x PSBC)	50,000	0.76583	65,289

Table 7 Phase three optimization results comparison

As can be seen from Table 7 above, the global mat strength was significantly increased in both comparative loading cases with the implementation of the proposed secondary beam component design. As the last part of this third step, global failure analysis must be included, represented by Figures 49 and 50 below. These figures represent approximated Von Mises Equivalent Stresses for the same models detailed above, units in pounds per square inch.

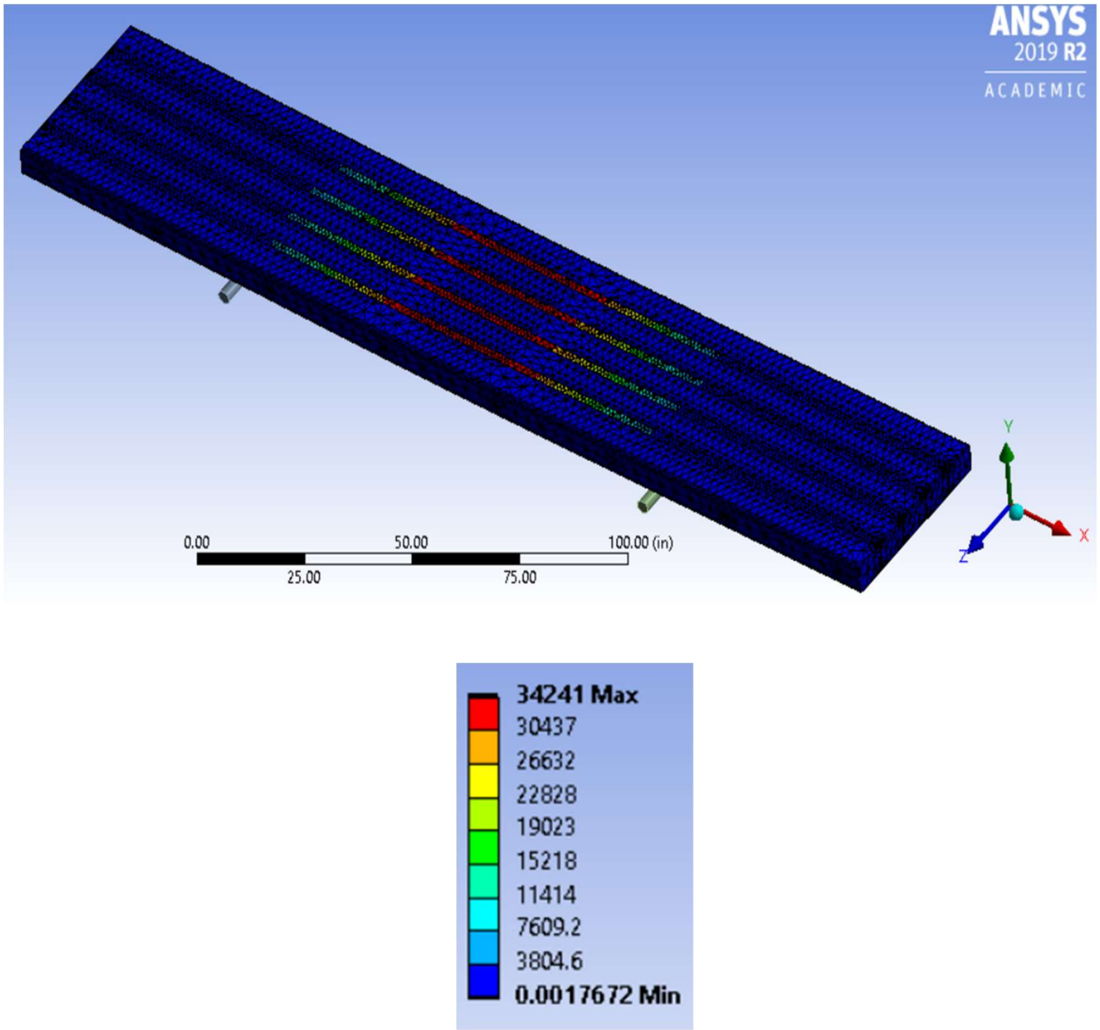

Figure 49 Phase three optimization, global numerical model, Von Mises equivalent stresses [psi], (7x9) x 5 x (4x¼) boundary conditions

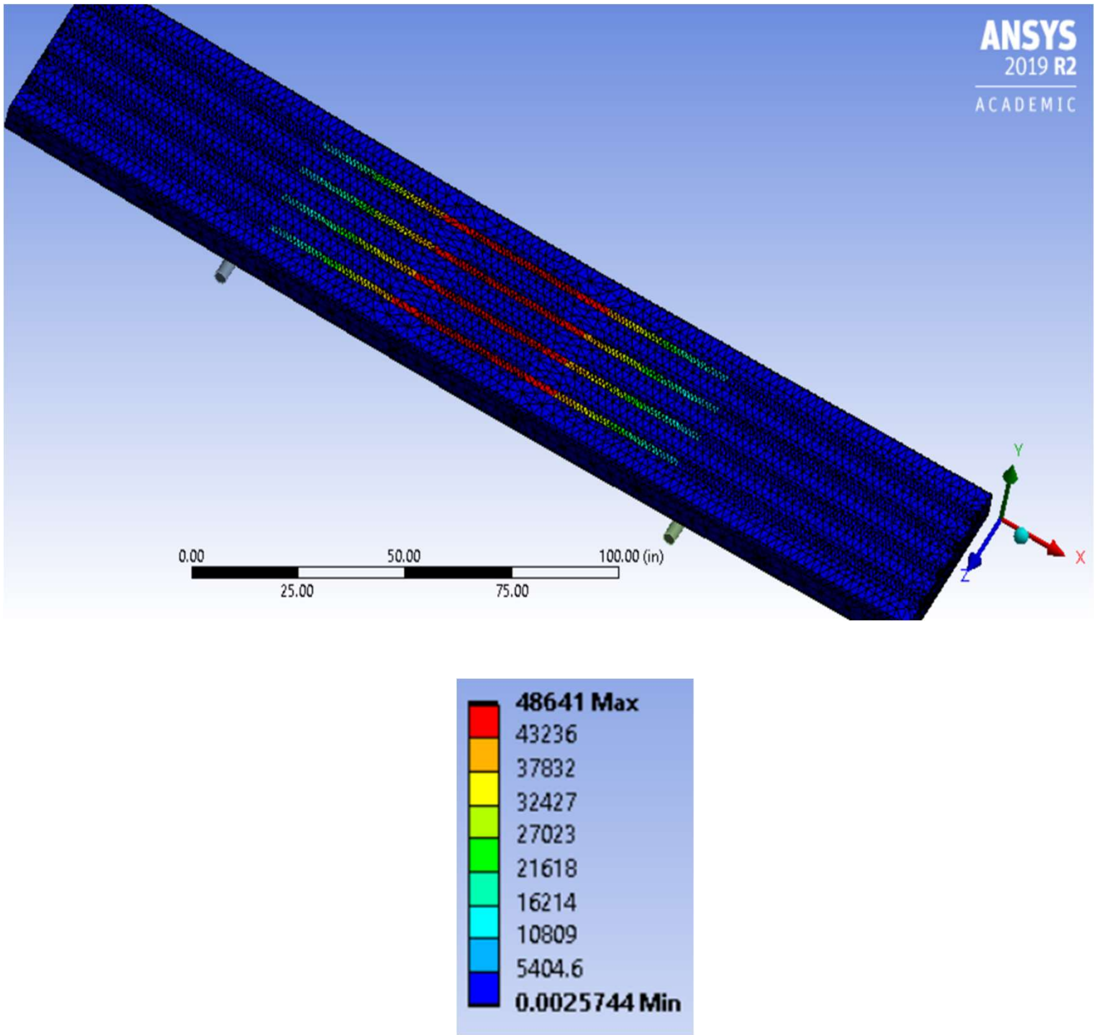

Figure 50 Phase three optimization, global numerical model, Von Mises equivalent stresses [psi], (7x9) x 5 x (4x½) boundary conditions

As can be seen from the figures above, while for the *(7x9) x 5 x (4x¼)* configuration load case, the proposed secondary beam component design was a useable and sufficient optimized design. Maximum global Von Mises stresses of about 34,000 [psi] occurred in the flanges of the secondary beam components, with the yield strength of A36 steel at 36,000 [psi]. However, for the *(7x9) x 5 x (4x½)* configuration load case, maximum global Von Mises stresses occurred in the same location but reached about 49,000 [psi], well beyond the yield strength of A36 steel. This indicated the proposed secondary beam component design would not be a sufficient replacement for the unoptimized secondary beam components within that configuration.

CONCLUSIONS

Modern construction mats and the advanced materials they are comprised of, present ample opportunity for optimization of structural design and by consequence, product cost. The above methodology established this concept, and detailed the groundwork necessary to complete such an analysis. A large variety of designs can be readily explored and developed without the need for further experimental testing.

While the tools developed and contained in this thesis represent the majority of the necessary procedure to manipulate and evaluate such a structure, it must be restated that depending on the design being evaluated, various local analysis of components may or may not be necessary. This would include for example, local buckling, and local and global fatigue life.

Some considerations are also deserving of mention as this research moves forward. First would be an in-depth look at the applied loadings to this structure. While the work in this thesis focused on replicating the experimental four-point bend test for modeling purposes, a study should be performed focusing on operational load cases for the structure. Namely, load cases representative of the structure's use in the field, so that driving cases could be established for proper redesign and optimization. This would include load cases across various pieces of equipment, i.e. excavators, cranes, trucks, etc. In addition, because these mats are placed in various locations with a wide range of soil conditions, the load cases would also have to include soil-spring boundary conditions, e.g. a Winkler model. Another area of exploration, one invoked in the research above, would be the method of fastening the beam components together into a plate structure. While largely outside the scope of analysis in the work above, the effects of partial interaction between beam components should be studied, and by association optimal component fastening.

REFERENCES

Allen, D.H. and Haisler, W.E., *Introduction to Aerospace Structural Analysis,* Wiley, 1985.

ANSYS. Inc. (2004). *ANSYS Contact Technology Guide*.

Blodgett, O. W. (1966). *Design of Welded Structures*. James F. Lincoln Arc Welding Foundation.

Forest Products Society. (2011). *Wood handbook: wood as an engineering material*. Madison, WI.

Ho, Qhinhon D., "An Assessment Of The Accuracy Of The Euler-Bernoulli Beam Theory For Calculating Strain and Deflection in Composite Sandwich Beams" (2015). University of New OrleansTheses and Dissertations. 2084.

Johnson, R. P., & Molenstra, I. N. (1991). Partial shear connection in composite beams for buildings. *Structural and Building Board*, 679–704.

Li, L. Z., Jiang, C. J., & Su, R. K. L. (2015). Simplified Flexural Design of Bolted Side-Plated Beams with Partial Interaction. In *6th International Conference on Advances in Experimental Structural Engineering*. University of Illinois, Urbana-Champaign.

Li, L. Z., Lo, S. H., & Su, R. K. L. (2013). Experimental Study of Moderately Reinforced Concrete Beams Strengthened with Bolted-Side Steel Plates. *Advances in Structural Engineering*, *16*, 499–516.

"MetalMiner Prices: Carbon Steel Prices." *North American Carbon Steel Price Index*, MetalMiner, 29 Aug. 2019, agmetalminer.com/metal-prices/carbon-steel/.

Miyamoto, Y. (1999). *Functionally Graded Materials Design, Processing and Applications*. Springer Science and Business Media.

Oehlers, D. J., Nguyen, N. T., & Ahmed, M. (1997). Transverse and longitudinal partial interaction in composite bolted side-plated reinforced-concrete beams. *Structural Engineering and Mechanics*, *5*, 553–563.